Free-surface deformation and air entrainment in turbulent flow past a rotating cylinder beneath a water–air interface

Citation for the original published paper (version of record):
Lin, J., Zhu, Z., Cao, X. et al (2026). Free-surface deformation and air entrainment in turbulent flow past a rotating cylinder beneath
a water–air interface. International Journal of Multiphase Flow, 203.
http://dx.doi.org/10.1016/j.ijmultiphaseflow.2026.105874

International Journal of Multiphase Flow 203 (2026) 105874

Contents lists available at ScienceDirect

International Journal of Multiphase Flow

journal homepage: www.elsevier.com/locate/ijmulflow

Research Paper

Free-surface deformation and air entrainment in turbulent flow past a rotating cylinder beneath a water–air interface

Jianfeng Lin [a], Zenghui Zhu [a,c], Xuxiang Cao [d], Lin Cai [e], Shizhao Wang [a,c], Hua-Dong Yao [b,*]

[a] The State Key Laboratory of Nonlinear Mechanics, Institute of Mechanics, Chinese Academy of Sciences, Beijing 100190, PR China
[b] Department of Mechanics and Maritime Sciences, Chalmers University of Technology, 412 96, Gothenburg, Sweden
[c] School of Engineering Sciences, University of Chinese Academy of Sciences, Beijing 100049, PR China
[d] National SuperComputer Center in Tianjin, Tianjin 300457, PR China
[e] College of Shipbuilding Engineering, Harbin Engineering University, Harbin 150001, PR China

HIGHLIGHTS

- Clockwise rotation drives deep waves and air mixing, unlike anticlockwise.
- Froude number thresholds control extreme air mixing and wave dynamics.
- Intense air entrainment severely reduces lift forces on rotating cylinders.
- An optimal shallow depth maximises lift by balancing wave and wake effects.

GRAPHICAL ABSTRACT

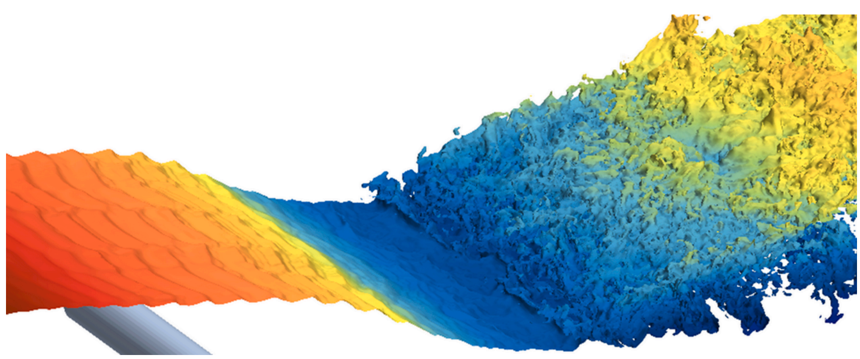

ARTICLE INFO

Keywords:
Magnus effect
Free surface
Air entrainment
Rotating cylinder
Volume of fluid
Wave breaking

ABSTRACT

The flow past a fully submerged rotating cylinder beneath a free surface involves complex multiphase interactions, including free-surface deformation, air entrainment, and wave breaking. Using large-eddy simulation coupled with the volume-of-fluid method, we investigate these phenomena at $Re = 6 \times 10^4$ and spin ratio $\alpha = 2$ over a range of submergence depths $H/D = 3$–100, Froude numbers $Fr = 2.0$–3.2, and both clockwise and anticlockwise rotations. The free surface exhibits markedly different responses depending on the rotation direction: clockwise rotation produces a deep wave trough accompanied by intense air entrainment, whereas anticlockwise rotation generates a wave crest with substantially less entrainment. The two-phase mixing region volume is quantified and found to exhibit local extrema, reflecting the shifting balance between gravity- and inertia-dominated regimes for the parameter set investigated. The lift coefficient exhibits a significant reduction that is strongly correlated with the occurrence of intense air entrainment, with an optimal submergence of $H/D = 5$ providing maximum lift under moderate Froude numbers. The streamwise velocity field reveals how air

* Corresponding author.
E-mail addresses: linjf@imech.ac.cn (J. Lin), zhuzenghui@imech.ac.cn (Z. Zhu), caoxx@nscc-tj.cn (X. Cao), cai_lin@hrbeu.edu.cn (L. Cai), wangsz@lnm.imech.ac.cn (S. Wang), huadong.yao@chalmers.se (H.-D. Yao).

https://doi.org/10.1016/j.ijmultiphaseflow.2026.105874
Received 1 June 2026; Received in revised form 25 July 2026; Accepted 30 July 2026
Available online 31 July 2026

entrainment alters the wake structure and promotes energy dissipation. These findings provide a fundamental quantitative understanding of multiphase Magnus-effect flows.

1. Introduction

Rotating cylinders are widely used in engineering applications, for example, ship anti-rolling devices and wind-assisted propulsion systems. Their operation relies on the generation of a lift force by cylinder rotation, known as the Magnus effect (Swanson, 1961; Seifert, 2012). This effect was originally identified in single-phase flows and has been extensively studied. In the case of ship anti-rolling devices, however, the cylinder operates beneath a free surface with air above the water. The presence of the free surface introduces additional flow interactions, which may modify the classical Magnus effect (Lin and Yao, 2023).

The classical Magnus effect in single-phase flows depends primarily on the Reynolds number (Re) and the spin ratio of the cylinder (α), which is defined as the ratio of the rotational speed to the inflow velocity. Early studies established theoretical frameworks for analysing the influence of the rotation on vortex shedding and hydrodynamic forces (Mittal and Kumar, 2003; Pralits et al., 2010; Lu et al., 2011; Radi et al., 2013). After that, Rao et al. (2013) found two steady states and examined their stability to perturbations at $Re < 400$ with $1.9 \leq \alpha \leq 6.5$, showing that increasing rotation affects transitional wake modes. By placing a small wire upstream to introduce asymmetry in the inflow, Rao et al. (2015) reported that subharmonic modes are triggered at low rotational speeds. At $Re < 500$ with $1.6 \leq \alpha \leq 6$, numerical simulations by Munir et al. (2019) reported the nonlinear amplification of paired-vortex formation and shear-layer intensification with increasing rotational speed. At the higher Reynolds number, $Re = 6 \times 10^4$, with $0.48 \leq \alpha \leq 0.6$, large eddy simulation (LES) by Cheng et al. (2018) identified a lift-crisis phenomenon associated with delayed boundary layer separation by the cylinder rotation. Complementary experiments by Chen and Rheem (2019) quantified the influence of the cylinder aspect ratio together with Re and α and identified distinct vortex-shedding regimes. Extending the configuration to inclined cylinders, Bourguet (2021) showed that the inclination significantly alters the wake stability characteristics.

For free-surface flows, stationary and rotating horizontal cylinders that are partially submerged in liquids have been investigated both numerically and experimentally (Ren et al., 2019; Hu et al., 2023). Due to the partial submergence, the cylinder rotation can induce significant gas entrainment. Experiments by Sharma et al. (2015) examined air entrainment into the liquid. Rana et al. (2016) simulated the air entrainment and the wrapping dynamics of the free surface near the cylinder using a finite volume method with the volume-of-fluid (VOF) method. Their study addressed the effects of liquid properties on the free-surface dynamics and found that air entrainment patterns are determined by the interplay between centrifugal forces and viscous damping. After that, Panda et al. (2022) classified entrainment regimes in terms of the submergence ratio for different gas-liquid pairs.

Fully submerged rotating horizontal cylinders remain relatively poorly understood, despite their application in ship anti-rolling devices (Lin et al., 2021, 2022). Lin and Yao (2023) investigated this configuration at low Reynolds numbers ($Re \leq 250$), where turbulence does not arise. Apart from this study, few studies have focused on such configurations. In the limit of quiescent liquids ($Re = 0$), Panda and Rana (2022) analysed air entrainment in the vicinity of the cylinder. A related problem was considered by Kumar et al. (2017), who investigated gas entrainment for counter-rotating horizontal cylinders.

In contrast, a more extensive set of results has been obtained for the fully submerged horizontal cylinders without rotation. Early work characterised the free-surface deformation and vorticity generation under steady inflow conditions (Daichin and Lee, 2004; Malavasi and Guadagnini, 2007; Feshalami et al., 2022; Zhao et al., 2024). Two-dimensional simulations at $Re = 180$ by Reichl et al. (2005) showed that increasing inflow velocity leads to pronounced surface deformation and strong surface vorticity, which alters the wake structure. The role of the submergence depth was later examined using a numerical method of smoothed particle hydrodynamics (SPH) by Bouscasse et al. (2017), who reported that surface-induced vorticity can suppress classical Kármán vortex shedding. Multi-solver benchmarks for viscous free-surface flows at similar Reynolds numbers were subsequently provided by Colagrossi et al. (2019), highlighting metastable wake states arising from nonlinear wake-surface interactions. Extensions to unsteady dynamics were considered by Gu et al. (2020), who investigated vortex-induced vibrations of a spring-mounted cylinder beneath a free surface and observed a reduction in vibration amplitude with increasing submergence depth. At the higher Reynolds number of $Re = 7550$, LES by Zhao et al. (2021) revealed three-dimensional asymmetries and jet-like flow structures between the cylinder and the free surface. More recently, Patel et al. (2025) examined the coupled dynamics of free-surface deformation and hydrodynamic forces, demonstrating the role of the Weber number and surface tension in determining lift generation.

Despite the extensive literature on stationary cylinders, the configuration of a fully submerged rotating horizontal cylinder at $Re = O(10^4)$ remains largely unexplored. To clarify the novelty of the present work, it is essential to distinguish it from previous studies. Firstly, compared to our previous low-Reynolds-number investigation (Lin and Yao, 2023), which was restricted to $Re \leq 250$ and laminar flow regimes, the present study addresses the high-Reynolds-number regime ($Re = 6 \times 10^4$). At this Re, the boundary layer is fully turbulent, leading to complex three-dimensional wake structures that are entirely absent at low Re. Secondly, while extensive research exists on stationary cylinders near a free surface (Reichl et al., 2005; Bouscasse et al., 2017; Zhao et al., 2021; Patel et al., 2025), the physics are predominantly governed by gap flow and surface-induced vorticity. The introduction of cylinder rotation fundamentally breaks this symmetry, coupling the Magnus effect with free-surface dynamics. Thirdly, unlike studies on partially submerged rotating cylinders (Rana et al., 2016), where the cylinder pierces the interface, the fully submerged configuration investigated herein features air entrainment driven by the depression of wave troughs rather than direct surface piercing.

Consequently, the primary novelties of this study are the simulation of the intricate coupling between high-Re turbulence, free-surface deformation, and air entrainment; the quantification of the two-phase mixing region volume, identifying specific Froude-number regimes that delineate variations between gravity-dominated and inertia-dominated flows; the revelation of a striking rotation-direction asymmetry, demonstrating that clockwise rotation induces a deep wave trough with intense air entrainment, whereas anticlockwise rotation generates a wave crest with negligible entrainment; and the elucidation of how these multiphase interactions profoundly degrade the lift coefficient.

The remainder of the paper is organised as follows. The problem formulation and numerical methodology are described in Section 2, together with validation and resolution studies. The results are presented and discussed in Section 3, including the effects of the submergence depth, Froude number, and rotation direction on the wake dynamics and hydrodynamic forces. Finally, the main conclusions are summarised in Section 4.

2. Problem setup and numerical method

2.1. Problem description

The configuration of the fully submerged rotating cylinder beneath a free surface is shown in Fig. 1. The coordinate system is defined with the freestream velocity U_0 along the positive X-axis, the vertical upward direction as the positive Z-axis, and the spanwise direction as the Y-axis. The clockwise (CW) rotation is defined such that the tangential velocity of the cylinder's upper surface is in the same direction as the freestream, generating an upward lift force. The anticlockwise (ACW) rotation is the reverse, where the upper surface moves against the freestream, generating a downward lift force. To facilitate a direct comparison of the force magnitude between the two rotation directions for engineering applications, the lift coefficient presented in this study is defined as the absolute value. The diameter of the cylinder is represented by D. The spanwise length is set to $L/D = 7$, according to the typical aspect ratio of Magnus anti-rolling devices (Lin et al., 2023, 2024). This choice is deliberately more conservative than the spanwise extent of $L/D = 3$ adopted in benchmark LES studies of rotating cylinders in single-phase flows at comparable Reynolds numbers (Cheng et al., 2018). The depth of the liquid is $10D + H$ with $H/D \in [3, 100]$, where H is the submergence depth defined as the distance from the centre of the cylinder to the initial free surface. The inlet of the computational domain is located $20D$ away from the cylinder centre, and the outlet position is $100D$. The top boundary in the gas is located $8D$ above the initial free surface. As verified by comparing different boundary distances in our previous works, the computational domain size adopted in this study is sufficient to exclude the blockage and shallow-depth effects.

Dimensionless parameters include the Reynolds number ($Re = \rho_w U_0 D/\mu_w$), the Froude number ($Fr = U_0/\sqrt{gD}$), the spin ratio ($\alpha = 0.5\omega D/U_0$), the submergence depth ratio (H/D), the density ratio ($\rho_w/\rho_a = 844.49$), and the viscosity ratio ($\mu_w/\mu_a = 61.40$). It is worth noting that for the two fluids, the densities (ρ_a and ρ_w) and the viscosities (μ_a and μ_w) are defined according to air and water. The freestream velocity U_0 is determined by $Re = 6 \times 10^4$. The rotational speed ω is from $\alpha = 2$, and the rotation direction is set to CW or ACW. To obtain a range of $Fr \in [2.0, 3.2]$ whilst maintaining a constant Reynolds number ($Re = 6 \times 10^4$), the gravitational acceleration g is adjusted, whilst the freestream velocity U_0 and fluid properties remain invariant. This numerical strategy is deliberately adopted to isolate the Froude-number effects from Reynolds-number dependencies, which are important at $Re = 6 \times 10^4$ where boundary layer separation and wake turbulence are highly sensitive to Re. Consequently, the Weber number ($We = \rho_w U_0^2 D/\sigma$, where σ is the surface tension) remains strictly constant and significantly greater than unity ($We \sim O(10^3)$ for macroscopic cylinder diameters), confirming that inertial forces overwhelmingly dominate surface tension. The Bond number ($Bo = \Delta\rho g D^2/\sigma$, where $\Delta\rho$ is the density difference between the two phases), which relates to the Froude and Weber numbers via $Bo = We/Fr^2$, varies with Fr but remains sufficiently large ($Bo \gg 1$) across the parameter space. This ensures that macroscopic free-surface dynamics and wave breaking are governed purely by the gravity-inertia balance, and the observed variations at specific Froude numbers are genuine physical phenomena rather than capillary or numerical artefacts.

2.2. Numerical method

2.2.1. Governing equations

Both fluids are assumed to be incompressible. The LES with implicit filtering is used to simulate the turbulent flow. The wall-adapting local-eddy viscosity (WALE) model is employed to determine the subgrid-scale (SGS) viscosity (Kim et al., 2020). While modern advanced models, such as the anisotropic minimum-dissipation model and the modulated gradient model, offer excellent performance for anisotropic turbulence, the WALE model is favoured in this study. It natively provides the correct near-wall scaling without requiring dynamic spatial averaging, which is highly advantageous for maintaining numerical stability near the sharp density gradients of the VOF free surface and within the complex moving overset mesh topology. The governing equations of the LES (Arya and De, 2019; Rodriguez et al., 2017) are given as follows:

$$\frac{\partial \widetilde{U}_i}{\partial x_i} = 0, \tag{1}$$

$$\frac{\partial \widetilde{U}_i}{\partial t} + \frac{\partial \widetilde{U}_i \widetilde{U}_j}{\partial x_j} = -\frac{1}{\rho}\frac{\partial \widetilde{P}}{\partial x_i} + \frac{\mu}{\rho}\frac{\partial^2 \widetilde{U}_i}{\partial x_j^2} - \frac{\partial \tau_{ij}}{\partial x_j} + f_i, \tag{2}$$

where $\widetilde{U}_i$ and $\widetilde{U}_j$ ($i, j = 1, 2, 3$) denote the filtered flow velocity components, x_i and x_j the components of the Cartesian coordinates, t the physical time, ρ the density of the fluid, $\widetilde{P}$ the filtered pressure, μ the dynamic viscosity, τ_{ij} the SGS stress tensor, and f_i a body force.

Eqs. (1) and (2) are solved using the finite-volume method and the semi-implicit method for pressure-linked equations (SIMPLE) algorithm. The mass-conservation constraint on the velocity field is enforced

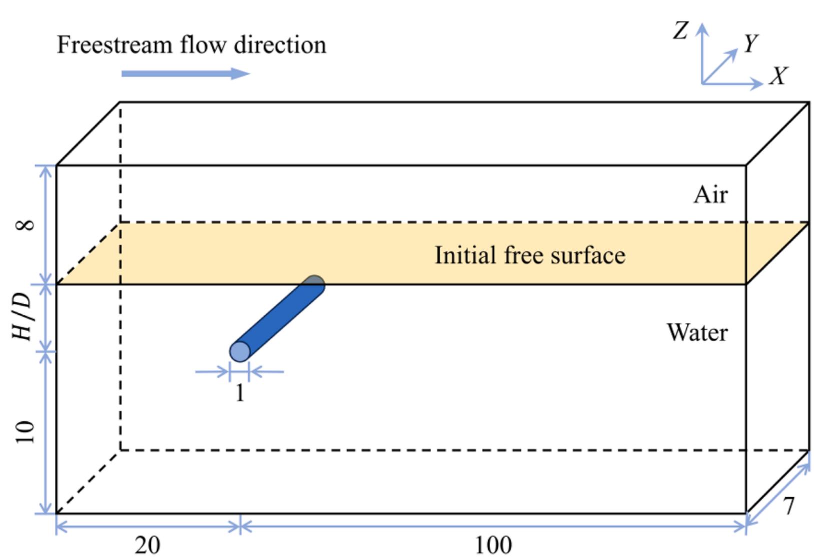

Fig. 1. Schematic of the computational setup.

through a pressure-correction equation. A bounded central-differencing scheme is used to discretise the convection term. An algebraic multigrid (AMG) method is employed to accelerate convergence of the solver. The first-order implicit Euler scheme is adopted for temporal discretisation. Although higher-order schemes introduce less temporal truncation error, the first-order scheme is selected to guarantee strict boundedness and numerical stability for the VOF interface amidst severe topological changes such as wave breaking.

2.3. VOF method

The free surface is captured using the VOF method (Hirt and Nichols, 1981). It enables the tracking of dynamic two-phase flow interfaces (i.e., the free surface) by introducing a scalar variable that represents the volume fraction of a given fluid with each cell. The volume fractions are continuous functions of space and time and sum to unity in each cell. This yields:

$$\lambda_a + \lambda_w = 1. \tag{3}$$

where λ_a and λ_w are the volume fractions of the gas and liquid.

The transport equations for the volume fractions have a similar structure for both phases. For the liquid phase, the equation is given by

$$\frac{\partial \lambda_w}{\partial t} + \frac{\partial \left(\lambda_w \widetilde{U}_j\right)}{\partial x_j} = 0. \tag{4}$$

In this study, phase change between the two phases is neglected. This assumption is justified because the simulations are performed under isothermal conditions with no thermodynamic driving forces, such as temperature gradients, superheating, or subcooling, that could induce evaporation or condensation. The gas and liquid phases are therefore treated as immiscible and incompressible, consistent with established numerical studies of air entrainment and rotating-cylinder free-surface flows (Rana et al., 2016; Colagrossi et al., 2019).

The density in each cell is given by

$$\rho = \lambda_a \rho_a + \lambda_w \rho_w, \tag{5}$$

where ρ_a and ρ_w denote the densities of the gas and liquid. The viscosity is also calculated in this way.

Considering Eq. (5), the momentum equations are written as:

$$\frac{\partial (\rho \widetilde{U}_i)}{\partial t} + \frac{\partial \left(\rho \widetilde{U}_i \widetilde{U}_j\right)}{\partial x_j} = -\frac{\partial \widetilde{P}}{\partial x_i} + \mu \frac{\partial^2 \widetilde{U}_i}{\partial x_j^2} - \frac{\partial \tau_{ij}}{\partial x_j} + \rho g + \sigma, \tag{6}$$

where σ denotes the interfacial surface tension force implemented based on the continuum surface force model (Brackbill et al., 1992; Zhou et al., 2019; Ferro et al., 2025). The velocity field $\widetilde{U}_i$ is shared by the phases.

The high-resolution interface-capturing (HRIC) scheme is employed together with the hydrostatic VOF wave model to accurately resolve the gas-liquid interface with a sharp representation (Chen et al., 2018; Wacławczyk and Koronowicz, 2008). The HRIC scheme blends bounded upwind and downwind differencing schemes for the advection of the volume fraction. Therefore, the scheme reduces numerical diffusion while maintaining boundedness of the volume-fraction field.

2.4. Numerical setup

The surface of the rotating cylinder is treated with a no-slip boundary condition. At the inlet of both phases, a velocity inlet boundary condition is prescribed, with turbulence characteristics specified according to the present Reynolds number (Gu et al., 2020; Reichl et al., 2005). The outlet is defined using a pressure-outlet boundary condition. The top boundary in the gas region and the bottom boundary in the liquid region are set with the symmetry condition. To reduce wave reflection at the domain boundaries, VOF wave damping (Choi and Yoon, 2009) is applied near the inlet, outlet, and side boundaries. This length scale is adopted to ensure consistent normalisation of characteristic scales and to suppress spurious reflections, as validated through preliminary numerical tests. The front and back boundaries of the computational domain are specified as symmetry planes. This treatment is adopted to accommodate the complex overset mesh topology and to strictly enforce a zero spanwise velocity gradient at the domain extremities. We conducted a sensitivity study of the segment lengths, such as $L/D = 2$, 3, 4, and 5, in the middle of the span. The results of the time-averaged and root-mean-square values of the hydrodynamic forces are consistent. This indicates that the symmetry plane has limited effects on the flow characteristics in the middle span region of interest. Therefore, the middle segment of $L/D = 3$ is chosen to extract and analyse the flow hydrodynamics.

The rotational motion of the cylinder is achieved using an overset mesh technique. The cylinder is positioned within a rotating overlapping mesh block that is overlaid on a background mesh covering the entire computational domain. The two mesh regions communicate across the overset interface through linear interpolation of flow variables between donor and acceptor cells, thereby coupling the solutions in the overlapping mesh regions.

As shown in Fig. 2, the diameter of the overlapping region is 5D. The overset mesh is structured with the maximum cell size of 0.04D. Here the cell sizes are presented for the medium mesh in Appendix A. To verify that the near-wall and wake turbulence are sufficiently resolved, the LES resolution metrics are monitored. The first-layer cell height near the cylinder wall is 0.00014D, ensuring a maximum dimensionless wall distance of $y^+ < 0.8$. The spanwise cell size is uniformly 0.04D, which is sufficient to resolve the spanwise coherence of the near-wall flows. The nominal filter width is highly anisotropic near the wall (0.006D) and approaches 0.04D in the wake. Crucially, the ratio of the SGS viscosity to the molecular viscosity is monitored and remains significantly less than unity in the boundary layer (approaching zero), peaking at approximately 3–5 in the wake. This confirms that the resolved scales dominate the energy-containing eddies, proving that the turbulence is adequately resolved.

The background mesh is unstructured and composed of trimmed cells. It has three refinement levels. The cell size near the domain boundaries is 0.16D. The maximum cell size of the finest level is the same as that of the overset mesh. The region of the finest level encloses the overset mesh so that the cell sizes match at the interface between the two meshes, ensuring consistent interpolation accuracy. Additional mesh refinement is applied in the vicinity of the free surface to improve the resolution of interfacial dynamics. The refinement region extends 1.28D in the vertical direction, with cell sizes ranging from 0.04D to 0.08D.

2.5. Validation

Owing to a lack of relevant experimental and numerical results for the current problem set-up in the literature, the methodology in this study is first validated against the rotating cylinder in single-phase flow at $Re = 6 \times 10^4$, $Fr = 3.2$, and $\alpha = 2$, for which comprehensive data have been reported by Swanson, (1961), Carstensen et al. (2014), and Cheng et al. (2018). Moreover, the mesh convergence is validated for the two-phase flow cases, taking into account the interface resolution (see Appendix A). For free-surface deformation, the VOF method is validated against the direct numerical simulations (DNS) data of a stationary cylinder near a free surface (Sun et al., 2025), showing excellent agreement for the wave profile with a root-mean-square error of <3% in the wave amplitude (see Appendix B). To validate the solver's capability to capture wave breaking and air entrainment, we perform quantitative comparisons with the DNS results of Deike et al. (2016) for three-dimensional breaking waves (see Appendix B). The validation focuses on the time evolution of entrained air volume during active breaking stages. Furthermore, the quantification of the two-phase mixing region relies on the mass conservation and interface sharpness of the

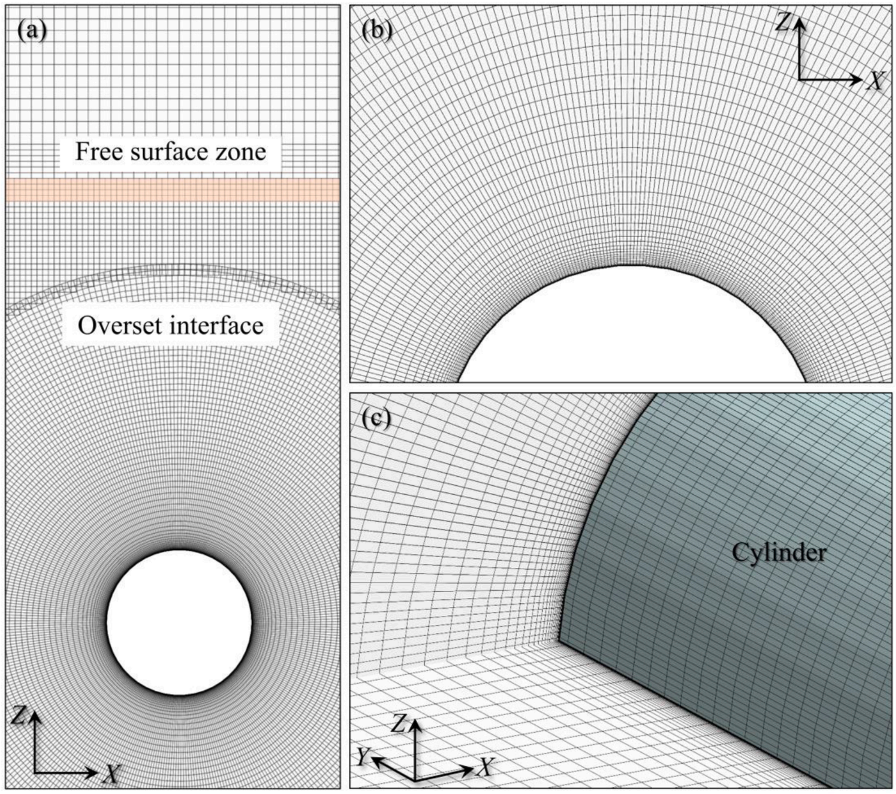

Fig. 2. Mesh cells: (a) near the free surface and the overset region; (b) and (c) near the walls shown in a cross-sectional plane and in an isometric view.

VOF method. The HRIC scheme maintains excellent mass conservation, with a relative mass error of <0.1% over the simulation time, ensuring the accurate prediction of the air entrainment.

To get sufficient mesh resolution with acceptable computational costs, a mesh convergence study was performed. To quantify the discretisation error, this work adopts the grid convergence index (GCI) approach, which is used in CFD verification studies (Park et al., 2015; Baker et al., 2020; Aycan et al., 2023). The GCI is presented as a percentage and represents a 95% confidence interval for the estimated discretisation error with a safety factor of 1.25. Three meshes were generated with the grid refinement ratio of $\sqrt{2}$, following the recommendation of the 2017 International Towing Tank Conference (ITTC).

The simulations are carried out for a sufficiently long period of time to allow the statistics to converge. The time-averaged lift coefficient, $C_l = \overline{F_z}/(0.5\rho_w LDU_0^2)$, and the time-averaged drag coefficient, $C_d = \overline{F_x}/(0.5\rho_w LDU_0^2)$, are obtained by averaging the lift and drag forces F_z and F_x over the last 50 periods, where one period corresponds to the time scale D/U_0. Here, the lift calculation excludes the buoyancy. To quantify the fluctuating behaviour, the root-mean-square values, $C_{l,rms}$ and $C_{d,rms}$, are also computed. Table 1 shows the results of the mesh convergence study. The present results show good agreement with the experimental data (Swanson, 1961; Carstensen et al., 2014) and the LES results reported by Cheng et al. (2018). The GCIs of C_l and C_d are <1.3%. Considering the large number of simulations needed, a mesh containing approximately 35 million cells is chosen as a reasonable compromise between numerical accuracy and computational costs after a thorough examination.

Based on the medium mesh, the sensitivity of the time-step size is investigated. Three different time steps are tested, corresponding to the rotational increments of 0.5°, 1°, and 2° of the cylinder per time step. The time steps satisfy two constraints: a maximum global convective Courant number smaller than 0.5, which is consistent with the temporal accuracy requirement for the LES; and a maximum capillary Courant number smaller than 0.25, which is the stability threshold for surface tension effects resolved using the continuum surface force model. For the largest time step, the maximum capillary Courant number is 0.18. Table 2 shows the relative errors of C_l and C_d below 1%. Considering the computational efficiency and solution accuracy, the time step corresponding to 1° of the cylinder rotations per time step is selected for the simulations in the following sections. Given the small time step employed, the temporal numerical dissipation is strictly bounded and remains negligible compared to the physical SGS dissipation.

3. Results and discussion

All the operating conditions in this study are listed in Table 3, comprising a total of 40 cases. The effects of the submergence depth, Froude number and rotation direction on the hydrodynamic characteristics of the rotating cylinder are analysed systematically.

Table 1
The results of the mesh convergence study.

Mesh	Total number of mesh cells (million)	C_l	GCI of C_l (%)	$C_{l,rms}$	C_d	GCI of C_d (%)	$C_{d,rms}$
Fine	49.39	4.711	0.61	0.15	0.318	0.75	0.059
Medium	35.28	4.736	1.30	0.15	0.319	1.20	0.059
Coarse	24.70	4.792	–	0.16	0.321	–	0.059

Table 2
The results of the time-step convergence study.

Rotating angle per time step	C_l	Relative error of C_l (%)	C_d	Relative error of C_d (%)
0.5°	4.664	–	0.520	–
1.0°	4.687	0.49	0.523	0.58
2.0°	4.705	0.88	0.525	0.96

Table 3
Summary of the operating conditions investigated in the present study.

Cases	H/D	Fr	Rotation direction
1–10	3, 5, 7.5, 10, 15, 20, 30, 40, 50, and 100	3.2	CW
11–20	3, 5, 7.5, 10, 15, 20, 30, 40, 50, and 100	3.2	ACW
21–30	3	2.0, 2.1, 2.2, 2.3, 2.4, 2.6, 2.7, 2.8, 3.0, and 3.2	CW
31–40	3	2.0, 2.1, 2.2, 2.3, 2.4, 2.6, 2.7, 2.8, 3.0, and 3.2	ACW

3.1. Effect of submergence depth on free-surface morphology

Fig. 3 shows the free-surface morphology at the mid-span section for different submergence depths. As the submergence depth increases, the influence of the cylinder on the free surface deformation diminishes. While the free surface and incoming flow interact with the upper surface of the cylinder, the CW cylinder rotation amplifies this effect at $H/D = 3$. The rotation accelerates the flow in the narrow region between the free surface and the upper surface of the cylinder. This acceleration produces a prominent local free-surface elevation in which part of the kinetic energy of the accelerated flow is converted into potential energy, resulting in an upstream elevation of the free surface. The remaining kinetic energy is dissipated through the turbulence. A similar local surface elevation induced by gap-flow acceleration was reported in the numerical study of a cylinder near a free surface by Bouscasse et al. (2017). As the submergence depth increases, the amplitude of the free-surface waves generated by the rotating cylinder progressively attenuates. For $H/D \gtrsim 30$, the free surface remains nearly undisturbed, indicating that its influence on the surrounding flow becomes negligible.

The instantaneous surface pressure coefficient, $C_p = (P - P_0 - \rho_w gh)/(0.5\rho_w U_0^2)$, as a function of the circumferential angle θ at the mid-span section for different submergence depths is shown in Fig. 4. Here P_0 denotes the atmospheric pressure of 1.01325×10^5 Pa, and h the vertical distance from a measurement point on the cylinder surface to the initial free surface (the still water level). The circumferential angle θ is defined in the $X - Z$ cross-sectional plane. The zero angle ($\theta = 0^\circ$) is located at the front stagnation point facing the incoming freestream, and the angle increases in the anticlockwise direction. Consequently, the lower and upper sides of the cylinder correspond to $\theta = 90^\circ$ and $\theta = 270^\circ$, respectively, while the rear stagnation point is located at $\theta = 180^\circ$. The results show that at $H/D = 3$, the C_p distribution on the cylinder surface differs from the other submergence depths. Specifically, relatively higher C_p are observed on the lower surface for $60^\circ \leq \theta \leq 180^\circ$, and notably higher near the upper surface at $\theta = 270^\circ$. This pressure pattern reduces the relative pressure difference between the upper and lower surfaces, resulting in a significant loss of the lift force. As the depth increases, the C_p on the upper surface decreases. Beyond $H/D > 7.5$, the minimum C_p stabilises around -6.5. Overall, the differences of the C_p distributions amongst the cases diminish with increasing submergence depth.

The streamlines for the instantaneous velocity fields of the horizontally rotating cylinder at different submergence depths are plotted in Fig. 5. It can be observed that the stagnation points of the incoming flow at different H are all located around $\theta = 20^\circ$, corresponding to the positive peak value of C_p in Fig. 4. The recirculation zones for different H lie within the angular range of 90° to 180° in the area of θ, corresponding to the plateau region where $C_p \approx 0$ in Fig. 4. An ACW near-wall vortex is present below the cylinder near $\theta = 90^\circ$. At $H/D = 5$, this vortex is closer to the wall, with the CW trailing-edge vortex near $\theta = 180^\circ$ disappearing. The incoming flow upstream of the stagnation point exhibits a similarly inclined upward direction in all cases. However, the wake deflection angle behind the cylinder varies with depth. When $H/D \geq 5$, this deflection angle initially increases and then decreases with rising H. In classical single-phase flows, a larger wake deflection angle typically corresponds to a stronger reactive lift force, consistent with Newton's third law and the momentum redistribution induced by the Magnus effect. At $H/D = 3$, although the deflection angle increases significantly, the lift force drops noticeably. This apparent departure from classical behaviour is fundamentally driven by the strong free-surface interaction and the resulting drastic variation in local fluid density. Firstly, regarding the wake momentum flux, intense air entrainment at $H/D = 3$ creates a massive two-phase mixing region. The local mixture density is drastically reduced due to the extremely low density of the entrained air.

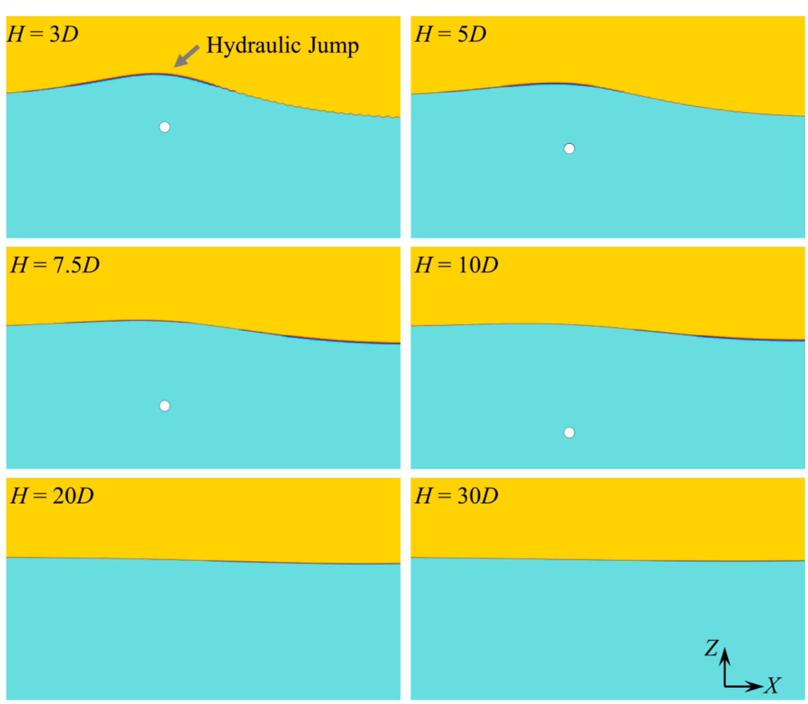

Fig. 3. Instantaneous morphology of the free surface influenced by the CW rotating cylinder at different submergence depths when $Fr = 3.2$.

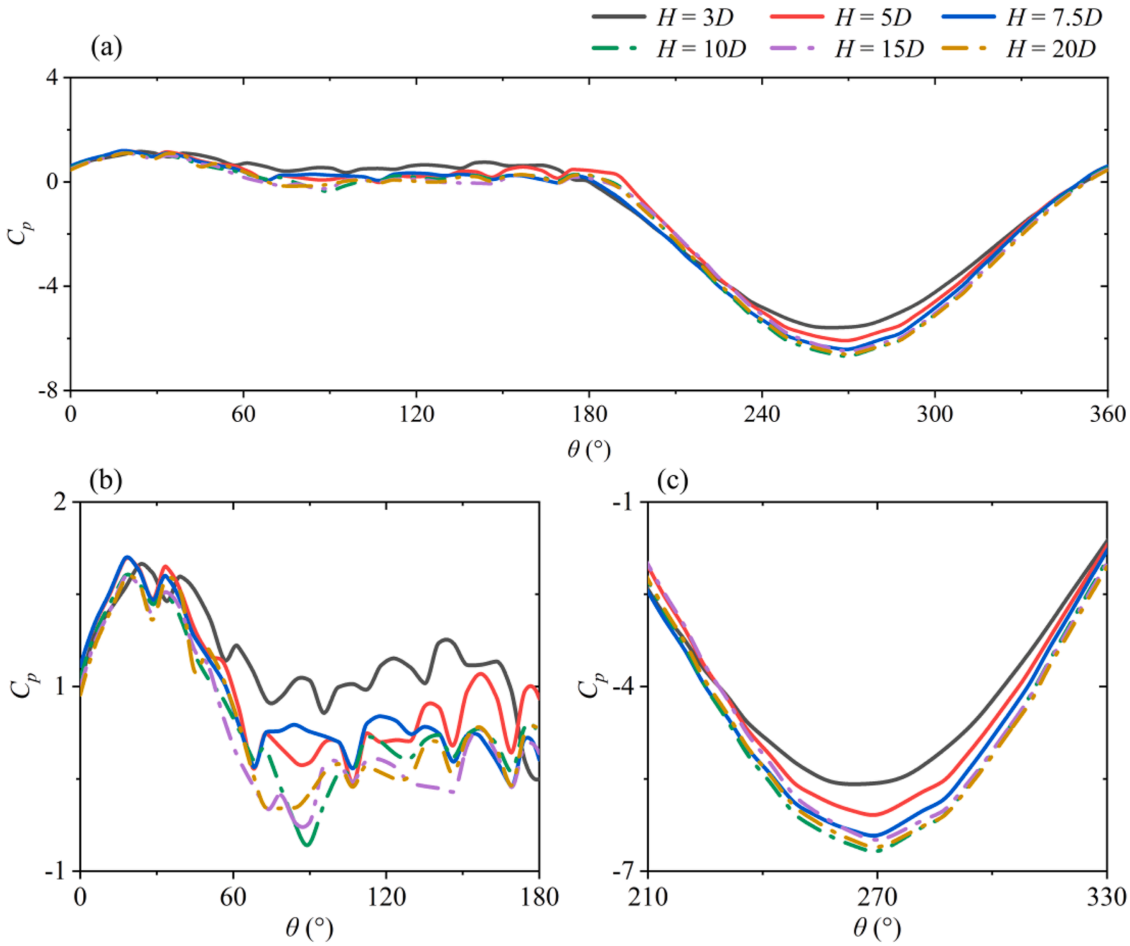

Fig. 4. Instantaneous surface pressure coefficient curves of the horizontally CW rotating cylinder at different submergence depths when $Fr = 3.2$: (a) $\theta \in [0^{\circ}, 360^{\circ}]$, (b) $\theta \in [0^{\circ}, 180^{\circ}]$, and (c) $\theta \in [210^{\circ}, 330^{\circ}]$.

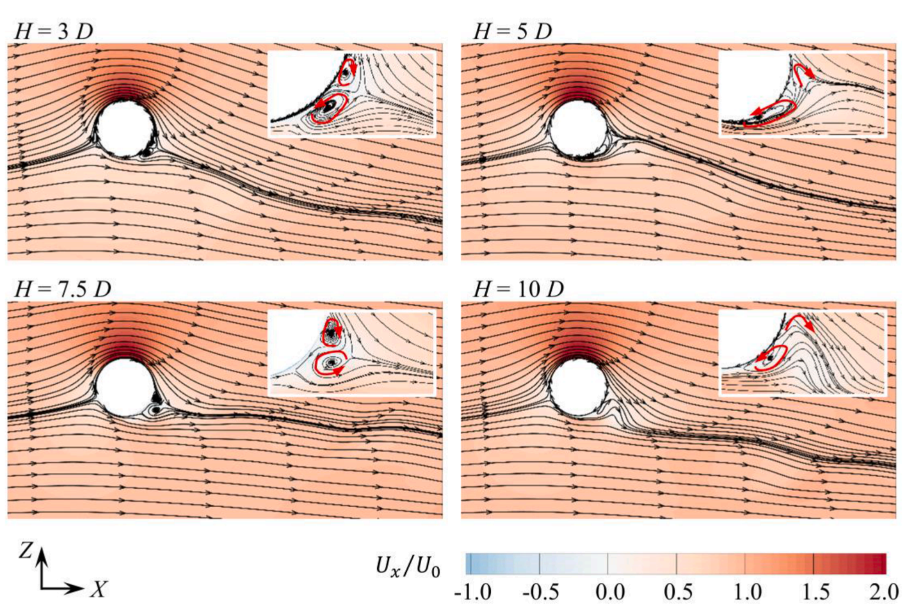

Fig. 5. Streamlines of the instantaneous velocity field of the horizontally CW rotating cylinder coloured by dimensionless streamwise velocity at different submergence depths when $Fr = 3.2$.

Consequently, although the wake exhibits a large geometric deflection angle, the actual momentum flux of the deflected fluid is significantly diminished. The large visual deflection is largely driven by the kinematic interaction with the highly deformable, low-density free surface, rather than a proportional reactive momentum transfer that generates lift. Secondly, regarding the surface pressure distribution and force decomposition, the entrainment of low-density air fundamentally alters the near-wake flow topology. The low-density two-phase mixture cannot sustain the severe pressure differential between the upper and lower surfaces as effectively as a single-phase liquid. As shown in Fig. 4, the minimum pressure coefficient on the suction side is elevated (i.e., its magnitude decreases). This reduction in the surface pressure differential directly leads to a significant loss of lift.

3.2. Effect of Froude number on air entrainment and wave dynamics

For a cylinder at $H/D = 3$ (close to the surface), the Froude number controls the balance between inertial and gravitational forces. The three-dimensional morphological properties of the free surface coloured with dimensionless vertical amplitude (A/D) at different Froude numbers are illustrated in Fig. 6. The vertical amplitude (A) is the difference between the coordinates in the Z-axis direction and the initial liquid level height. The free surface is affected by the horizontal cylinder's CW rotation, generating a deep wave trough at the backside of the cylinder and inducing intense air entrainment within the trough when $Fr = 2.2$. The continual intense interfacial shearing, violent wave breaking, and chaotic multiphase mixing cause a substantial amount of mechanical energy to be dissipated. This intense multiphase mixing and air entrainment are strongly correlated with a significant alteration of the surface pressure distribution (Fig. 9), which in turn leads to a degradation of the lift force (Fig. 11). As the Froude number increases beyond $Fr = 2.7$, the trough becomes shallower and the air entrainment subsides. This suppression of air entrainment is driven by the strong convective advection at high Fr, which kinematically elongates and shallows the wave trough, preventing it from penetrating deep enough to interact with the low-pressure core of the cylinder's wake. Without this low-pressure suction to induce interfacial instability, the wave breaking and air entrainment are physically suppressed.

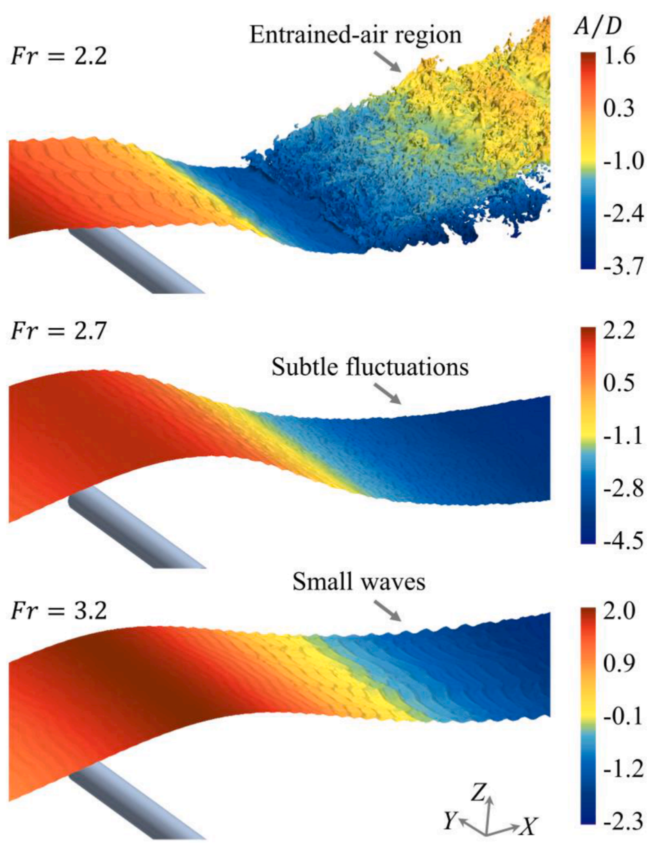

Fig. 6. Instantaneous three-dimensional morphological properties of the free surface, defined by an isosurface with a volume fraction of water equal to 0.5, are coloured with the dimensionless vertical amplitude (A /D) at different Froude numbers for the CW rotating cylinder when $H/D = 3$.

Fig. 7 shows the free-surface morphology generated by the horizontally rotating cylinder across the range of tested Froude numbers. With increasing Fr, its influence in the far field ($X/D \approx 100$) grows progressively stronger. In the near field ($X/D \approx 0$), the cylinder directly elevates the water surface, forming a distinct wave crest—driven by the flow acceleration-induced surface elevation shown in Fig. 3. As Fr rises, the first crest shifts closer to the cylinder and increases in amplitude. Conversely, the first trough moves farther downstream, with its amplitude initially increasing before decreasing. For $Fr \le 2.4$, intense air entrainment occurs at the first trough (see Fig. 6), which coincides with a marked reduction in lift and an increase in drag. The far-field wave peak for $Fr = 2.8$ exceeds the near-field surface elevation driven by the flow acceleration, a feature driven by the following key hydrodynamic processes. Air entrainment and near-field wave energy dissipation cease for $Fr \ge 2.7$, allowing nearly all wave energy generated by wake-free surface coupling to be preserved in propagating surface gravity waves. Specifically, the cessation of violent topological interface breaking removes a major energy sink, allowing the large-scale coherent wake vortices to efficiently transfer their kinetic energy to the free surface via unsteady pressure fluctuations and Reynolds stress work. The reduced local wave dissipation allows these surface gravity waves to propagate downstream with sustained amplitudes, explaining the enhanced far-field undulation observed at high Fr (Fig. 7).

The dimensionless streamwise velocity fields in the wake (Fig. 8) provide complementary insight. When $Fr \le 2.4$, intense air entrainment occurs in the troughs, accompanied by marked reverse flow. As Fr increases further, the counter-flow weakens and shifts downstream. At higher Fr, coupling between the submerged wake and the free surface weakens significantly compared to lower Fr conditions. This results in shallower surface troughs and longer associated wavelengths. Elongated wavelengths generally indicate reduced wave dissipation, explaining the sustained free-surface undulation observed in the far field ($X/D \approx 100$) at high Fr. In addition, increasing Fr enhances the tangential velocity at the first crest above the cylinder, raising the local water level under combined surface-tension effects.

The distribution of the surface pressure coefficient C_p in Fig. 9a reveals how these changes in free-surface and wake morphology translate into force variations. Since the hydrodynamic forces are the direct surface integrals of the pressure and viscous stress fields, the alteration of the C_p distribution by the multiphase mixing is the direct physical mechanism responsible for the observed degradation of the lift force. The C_p curve exhibits a single trough, reflecting the influence of vortex shedding from the cylinder on the surface pressure. At lower Froude numbers ($Fr < 2.6$), the angle-averaged pressure coefficient $\overline{C}_{p,\theta}$ on the lower cylinder surface ($\theta \in [60^\circ, 180^\circ]$) is smaller than that obtained at higher Fr; this difference is most pronounced at $Fr = 2.0$, as shown in Fig. 9b. In contrast, the minimum C_p on the upper surface increases more strongly with Fr (see Fig. 9c), resulting in a reduced pressure differential between the upper and lower surfaces and, consequently, a diminished lift. The angular location θ of the upper-surface minimum C_p shifts with Fr (see Fig. 9d). For $Fr \le 2.6$, the minimum occurs near $\theta \approx 253^\circ$, closer to the trailing edge. As Fr increases beyond 2.6, the minimum moves toward $\theta \approx 265^\circ$, the pressure differential recovers, and the pressure distribution approaches that of a rotating cylinder in the absence of severe free-surface interference.

3.3. Effect of rotation direction: trough vs. crest

In the first two subsections, the rotation direction of the cylinder was always CW, and in this subsection, the effects of the opposite rotation direction are compared and analysed. The distributions of the C_l and C_d

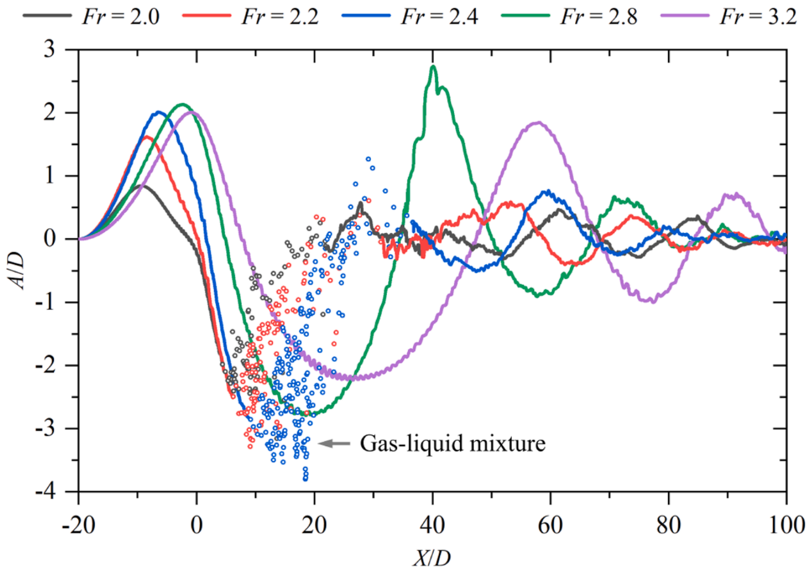

Fig. 7. Instantaneous morphological properties of the free surface influenced by the CW rotating cylinder at $H/D = 3$ with different Froude numbers.

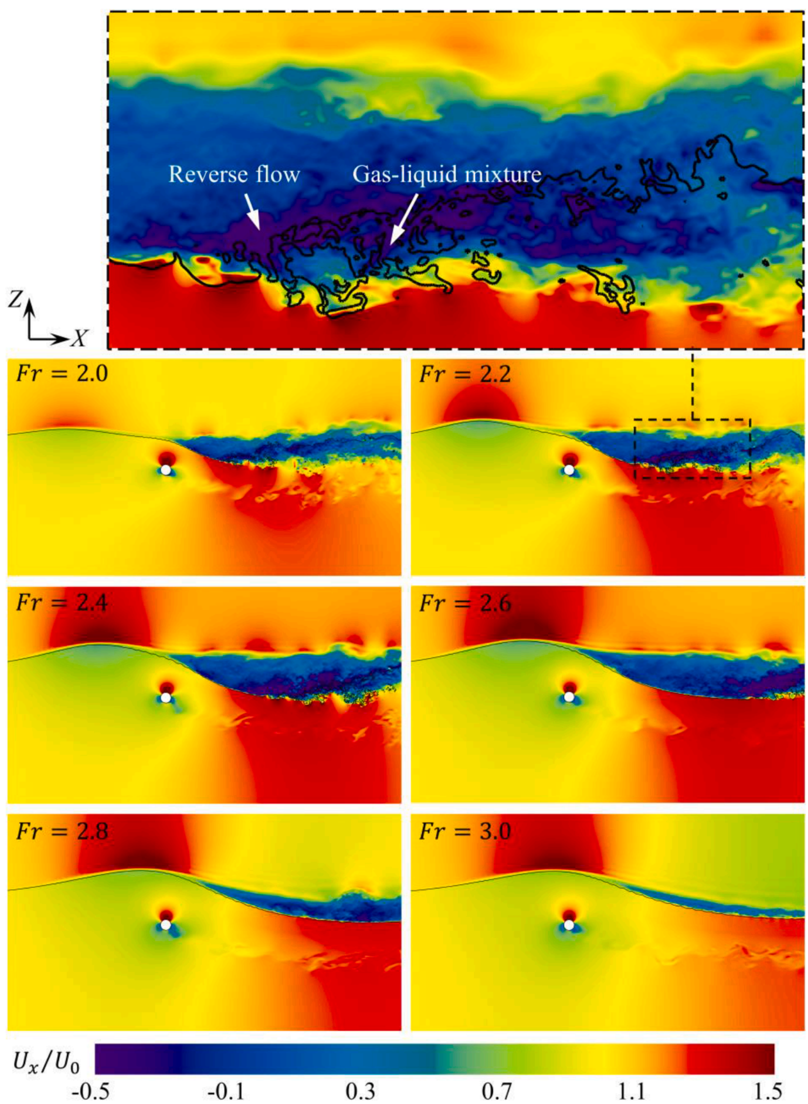

Fig. 8. Instantaneous trailing field of the horizontally CW rotating cylinder with dimensionless streamwise velocity at different Froude numbers when $H/D = 3$.

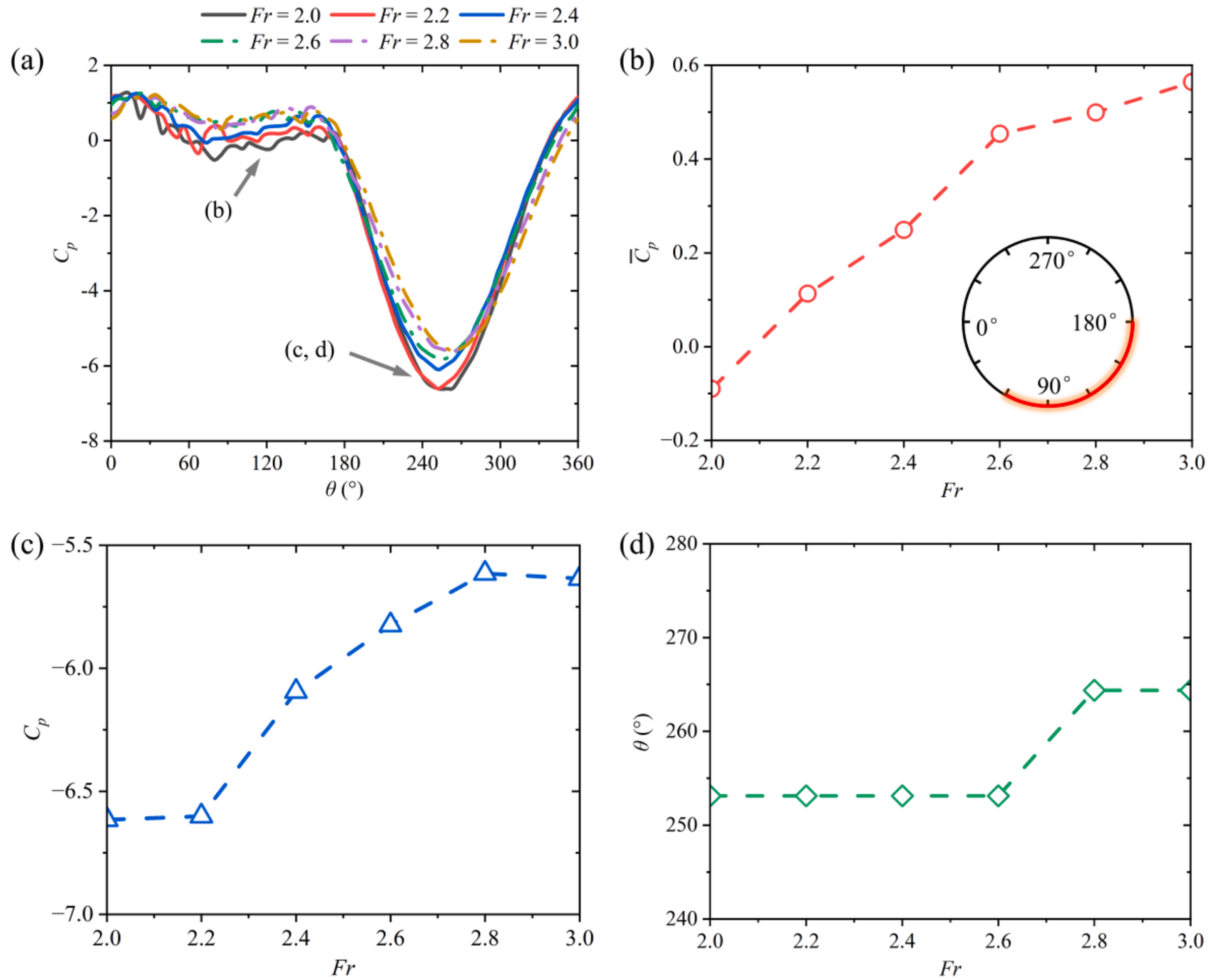

Fig. 9. Surface pressure coefficient curves of the horizontally CW rotating cylinder at different Froude numbers when $H/D = 3$. (a) Instantaneous circumferential distribution of C_p, (b) angle-averaged pressure coefficient $\overline{C}_{p,\theta}$ evaluated over the angular range $\theta \in [60^{\circ}, 180^{\circ}]$, (c) minimum instantaneous C_p magnitude, and (d) circumferential angular position corresponding to the minimum instantaneous C_p.

for the cylinder under different rotation directions, *Fr*, and H/D are presented in Figs. 10 and 11. As shown in Fig. 10a, under ACW rotation, C_l increases monotonically with *Fr*, stabilising for $H/D > 10$. At $H/D = 3$, strong interference from the free surface results in comparably low C_l values for both rotation directions. Near $H/D \approx 5$, the ACW case exhibits a marked reduction in C_l in close proximity to the free surface, which is consistent with the wall-effect observations of Cheng and Luo (2007). By $H/D \approx 10$, ACW rotation yields a higher C_l than CW rotation, although

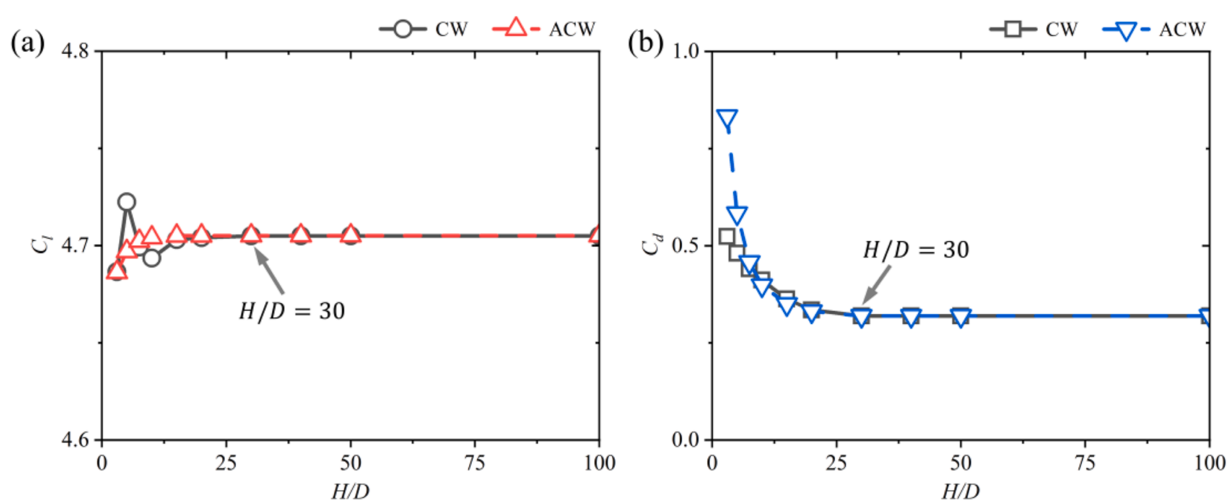

Fig. 10. a) The time-averaged lift coefficient and (b) the time-averaged drag coefficient at different rotation directions and submergence depths for the horizontally rotating cylinder when $Fr = 3.2$.

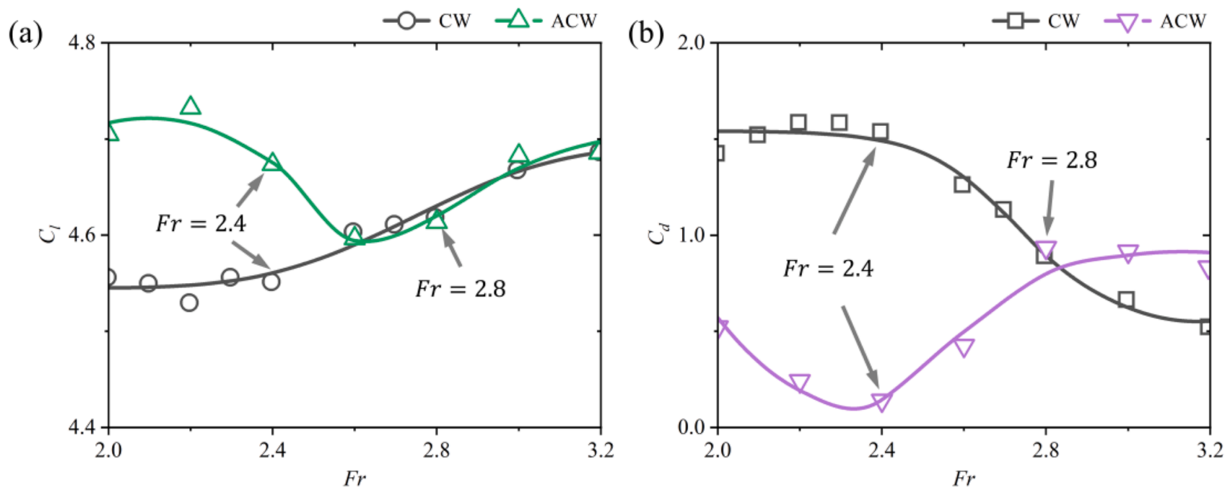

Fig. 11. (a) The time-averaged lift coefficient and (b) the time-averaged drag coefficient at different rotation directions and Froude numbers for the horizontally rotating cylinder at $H/D = 3$.

this difference gradually diminishes for $H/D > 15$ as the influence of the free surface weakens. In Fig. 10b, the rotation direction affects C_d only for $H/D < 7.5$, where ACW rotation produces higher drag. For $H/D \geq 7.5$, the C_d curves for the two directions converge. Fig. 11a demonstrates that, for $Fr \leq 2.6$, ACW rotation results in a higher C_l than CW rotation, maintaining a stable elevated level when $Fr < 2.4$—an outcome attributed to the combined effects of the free surface and the Magnus effect. For $Fr \geq 2.6$, however, the free-surface disturbance becomes weak, and the C_l values for both rotation directions equalise. Finally, Fig. 11b shows that C_d first decreases and then increases with increasing Fr, reaching a minimum near $Fr \approx 2.4$. Beyond $Fr = 2.8$, ACW rotation again yields a higher C_d than CW rotation.

The morphological characteristics of the free surface affected by an ACW rotation of the horizontal cylinder at various Fr and H/D are illustrated in Fig. 12. When the cylinder rotates ACW, the upper surface moves against the incoming flow, reducing the relative velocity near the free surface. This suppresses flow acceleration-induced surface elevation formation—a contrast to the CW case shown in Figs. 3 and 7. A wave crest develops behind the cylinder, rather than the trough observed for CW rotation. At $Fr = 3.2$ and $H/D = 3$, the free surface forms a small trough followed by a large downstream crest. As H increases, surface influence weakens: the trough vanishes and the crest attenuates, correlating with lower drag (see Fig. 10). For $H/D = 3$ and $Fr = 2.0$, a sharp crest with small apical curvature forms behind the cylinder, indicating incipient wave breaking. Within $2.2 \leq Fr \leq 2.6$, wave crests break, dissipating energy and reducing both lift and drag. At higher Fr,

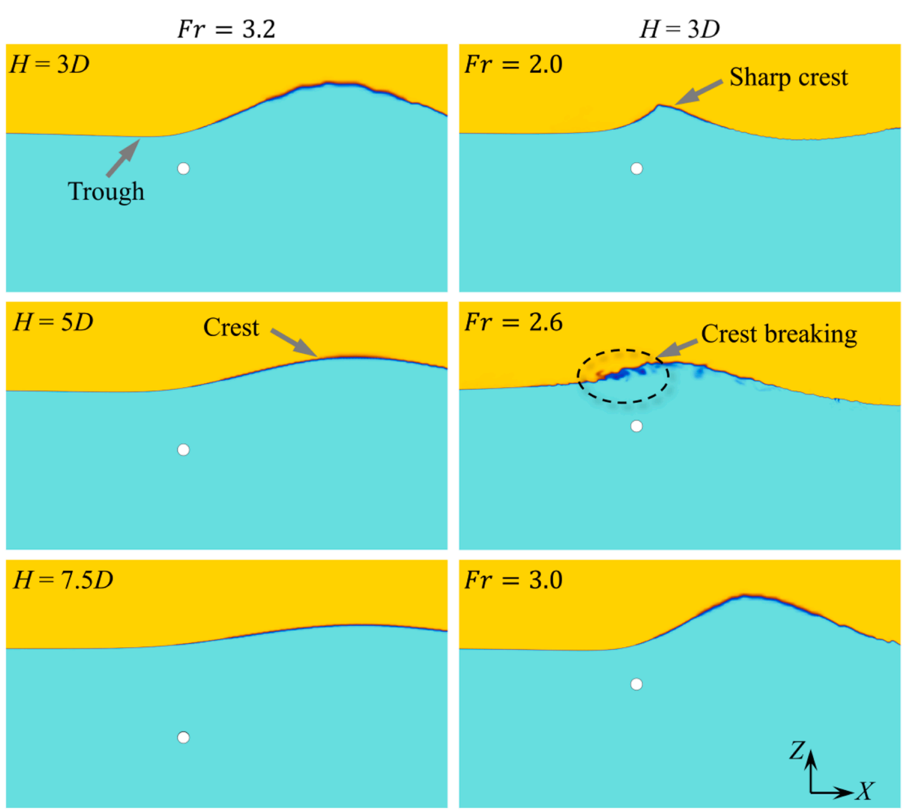

Fig. 12. Instantaneous morphological properties of the free surface influenced by the ACW rotating cylinder at different submergence depths and Froude numbers.

ACW rotation produces taller wave crests, significantly increasing drag (see Fig. 11). For $Fr \geq 2.6$, crest breaking ceases. The crests shift downstream, reducing their vertical influence on the cylinder and allowing lift to gradually increase, as shown in Fig. 11.

To quantify the intensity of air entrainment, the dimensionless two-phase mixing volume, V_h/V_0 (V_0 denotes the reference volume, i.e., the displaced volume of the cylinder), is employed as the primary metric. Physically, the dimensional volume V_h represents the total mixture volume within the domain. V_h is calculated as the volume integral where the water volume fraction satisfies $0.0001 \leq \lambda_w \leq 0.9999$. This threshold isolates the dispersed bubbles, entrained air cavities, and the fragmented interface from the bulk single-phase regions. While VOF excels at resolving large-scale interface topology and macroscopic air entrainment, it cannot resolve the subgrid-scale dispersed micro-bubbles generated during violent wave breaking. The region defined by the volume-fraction thresholds ($0.0001 \leq \lambda_w \leq 0.9999$) thus encompasses both the physically entrained macroscopic air cavities and the numerically resolved interfacial transition zone. Consequently, V_h/V_0 serves as a robust macroscopic proxy for the spatial extent and intensity of the multiphase mixing region, rather than a precise measure of the micro-bubble population. Furthermore, to ensure that the observed trends in V_h/V_0 are physically driven and not strongly dependent on the interface resolution, refer to the dedicated interface convergence study in Appendix A.

Fig. 13 presents a quantitative comparison of the V_h/V_0 as a function of the submergence depths and Froude numbers for both directions of cylinder rotation. As shown in Fig. 13a, V_h/V_0 differs markedly between the CW and ACW rotation directions at the smallest submergence $H/D = 3$. For $H/D \geq 5$, however, the results for the two rotating directions become similar, and V_h/V_0 is then dominated by the mixed volume at the two-phase interface. Irrespective of whether the cylinder rotates CW or ACW, two distinct inflection points are consistently observed on the curves, corresponding to $Fr = 2.4$ and $Fr = 2.8$ (see Fig. 13b). Notably, these two Froude numbers coincide with the inflection points identified on the lift and drag coefficient curves in Fig. 11. This close correspondence indicates that the generation of the air entrainment is a key factor influencing the lift and drag behaviour of a rotating cylinder. It should be emphasised that these specific Froude numbers represent local extrema observed for the present parameter set ($Re = 6 \times 10^4$, $\alpha = 2$, and $H/D = 3$), rather than universal critical thresholds.

The surface pressure coefficients for the ACW rotating cylinder are extracted for various Fr and H/D, and the results are presented in Figs. 14 and 15. Comparison of Figs. 4, 9, 14, and 15, reveals that reversing the rotation direction leads to an inverted pressure distribution on the upper and lower sides of the cylinder; the low-pressure interval (the trough of the curve) now appears on the lower side (near $\theta = 90^\circ$), producing a downward lift force. For the ACW rotating cylinder at $Fr = 3.2$, variations in immersion depth have negligible influence on the minimum value of C_p (see Fig. 14c). Only at $H/D = 3$ does the angular position θ corresponding to the minimum C_p shift from approximately 90° to roughly 96°, as shown in Fig. 14d. It is noteworthy that the circumferential angular positions of the minimum C_p for CW and ACW rotations are symmetric, yet the minimum C_p values differ markedly, especially for $H/D \leq 5$. A plateau of $C_p \approx 0$ is observed on the upper surface over $180^\circ \leq \theta \leq 300^\circ$ (Fig. 14a), coincident with the vortex reattachment location. For $H/D < 10$, the rotation direction significantly affects the $\overline{C}_{p,\theta}$. At $H/D = 3$, changes in Fr have a pronounced influence on both the magnitude and the location of the minimum C_p, as shown in Fig. 15. Over the range $2.2 \leq Fr < 2.8$, $\overline{C}_{p,\theta}$ and the minimum C_p are similar for the two rotation directions. For $Fr \leq 2.2$ and $Fr > 2.8$, corresponding to the higher C_d regime in Fig. 11b, the angular position of the minimum C_p increases from around 90° to approximately 96° (see Fig. 15d). This angular shift is roughly 6°, which is notably smaller than the 11° shift observed for the CW rotation.

4. Conclusions

For the investigated high Reynolds number ($Re = 6 \times 10^4$), the multiphase flows present complex mechanisms in relation to turbulence, air entrainment, and unsteady wave dynamics, which differ markedly from the laminar or transitional regimes observed at low Reynolds

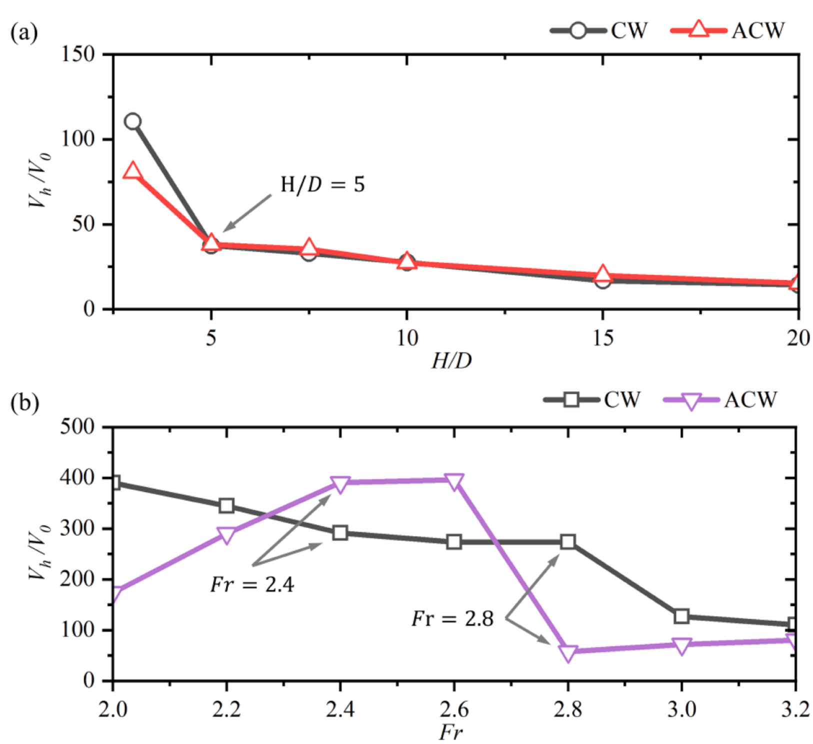

Fig. 13. The time-averaged dimensionless two-phase mixing volume varies with two rotational directions at different submergence depths and Froude numbers when (a) $Fr = 3.2$ and (b) $H/D = 3$.

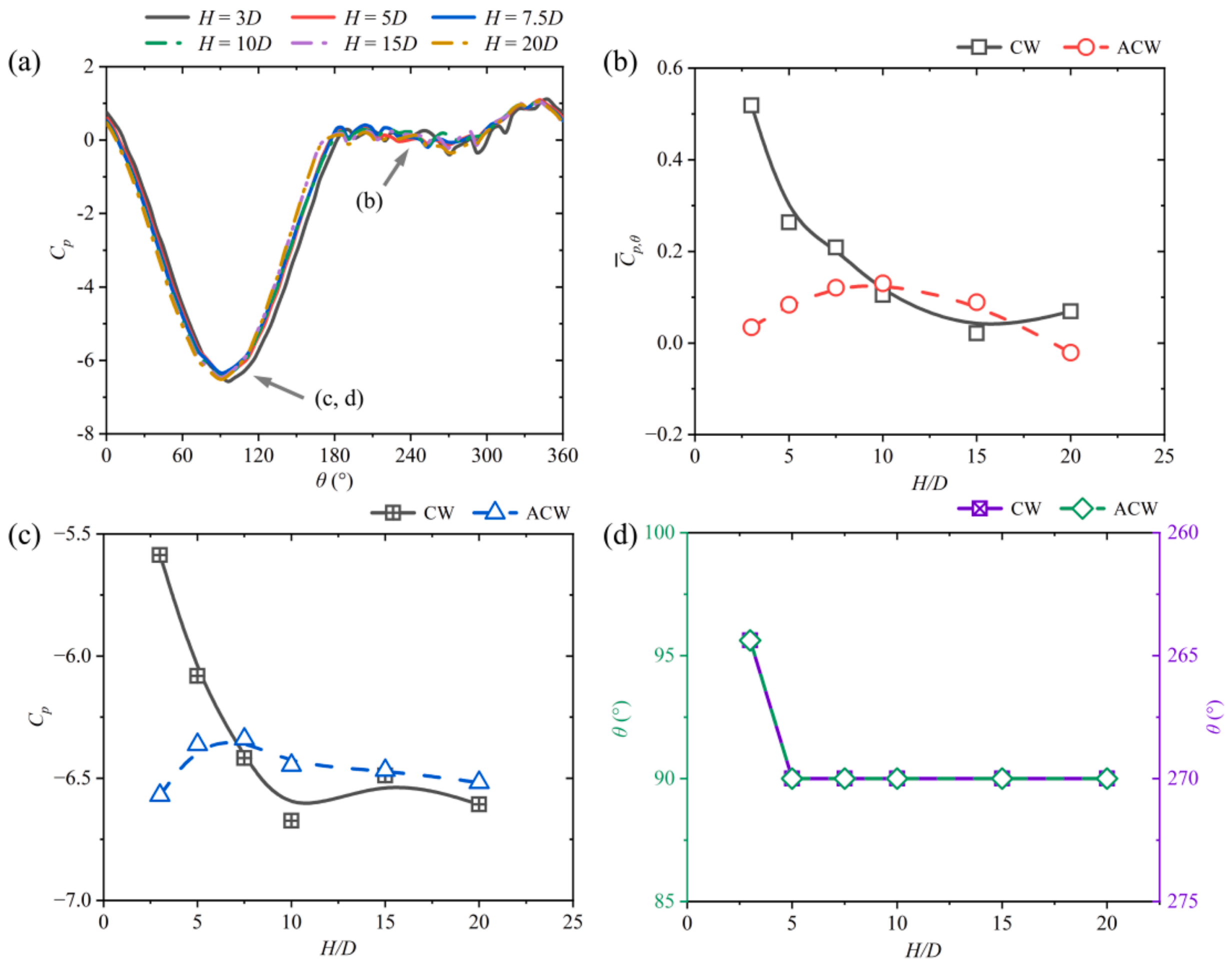

Fig. 14. Surface pressure coefficient distributions for the ACW rotating cylinder at different submergence depths for $Fr = 3.2$. (a) Instantaneous circumferential distribution of C_p, (b) angle-averaged pressure coefficient $\overline{C}_{p,\theta}$ evaluated over $\theta \in [180^{\circ}, 300^{\circ}]$, (c) minimum instantaneous C_p magnitude, and (d) circumferential angular position corresponding to the minimum instantaneous C_p.

numbers.

- Within the explored parameter space, the free-surface morphology exhibits a strong dependence on submergence depth and Froude number. Specifically, at the shallowest depth examined ($H/D = 3$), CW rotation induces a deep wave trough accompanied by intense air entrainment, whereas ACW rotation generates a wave crest with substantially less entrainment. For $H/D \geq 30$, the free surface remains virtually undisturbed under the present flow conditions.
- Air entrainment, quantified by the two-phase mixing volume, reaches two distinct inflection points at $Fr = 2.4$ and $Fr = 2.8$ for both rotation directions. For the present parameter set, local extrema are observed near these values, reflecting shifts in the balance between gravity-dominated and inertia-dominated regimes that coincide with inflection points in the lift and drag coefficients.
- The time-averaged lift coefficient demonstrates a non-monotonic dependence on H/D, reaching a maximum at $H/D = 5$ under the current conditions. At shallow depths, the lift is significantly reduced, a phenomenon that is strongly correlated with intense air entrainment and wake disruption. For instance, at $H/D = 3$ and $Fr = 2.2$, the lift loss exceeds 11% compared to the single-phase flow baseline.
- The rotation direction induces markedly asymmetric free-surface responses: a trough for CW rotation and a crest for ACW rotation. Under the investigated low Froude numbers, ACW rotation generally yields a higher lift magnitude than CW rotation, as the formation of a wave crest appears to be less dissipative than the intense multiphase mixing within a deep wave trough.
- The resolved velocity fields indicate that the observed air entrainment is closely associated with strong interfacial shear and reverse flow within the wave trough. Furthermore, the transition from chaotic to more organised wake dynamics with increasing Fr appears to be intrinsically linked to the suppression of this air entrainment.

Before extrapolating the present findings to practical marine engineering, several limitations of this idealised study must be recognised. First, the investigation is confined to a single Reynolds number ($Re = 6 \times 10^4$) and a single spin ratio ($\alpha = 2$), whereas actual marine devices operate over a broad parameter space in which boundary-layer separation and wake turbulence are highly sensitive to both quantities. Second, the simplified geometry assumes a uniform oncoming flow and a quiescent free surface, thereby neglecting the incident waves, hull boundary layers and cross-flow effects that characterise realistic ocean environments. Finally, the Froude number was varied by artificially adjusting the gravitational acceleration to decouple its influence from that of the Reynolds number; in practical applications, a change in flow velocity would simultaneously alter multiple dimensionless groups, so the specific Froude numbers identified here should be interpreted as fundamental thresholds in a decoupled parameter space. Future work will extend this framework to encompass a range of Reynolds numbers, spin ratios, and the influence of incident waves and hull boundary layers, thereby bridging the gap between fundamental fluid mechanics

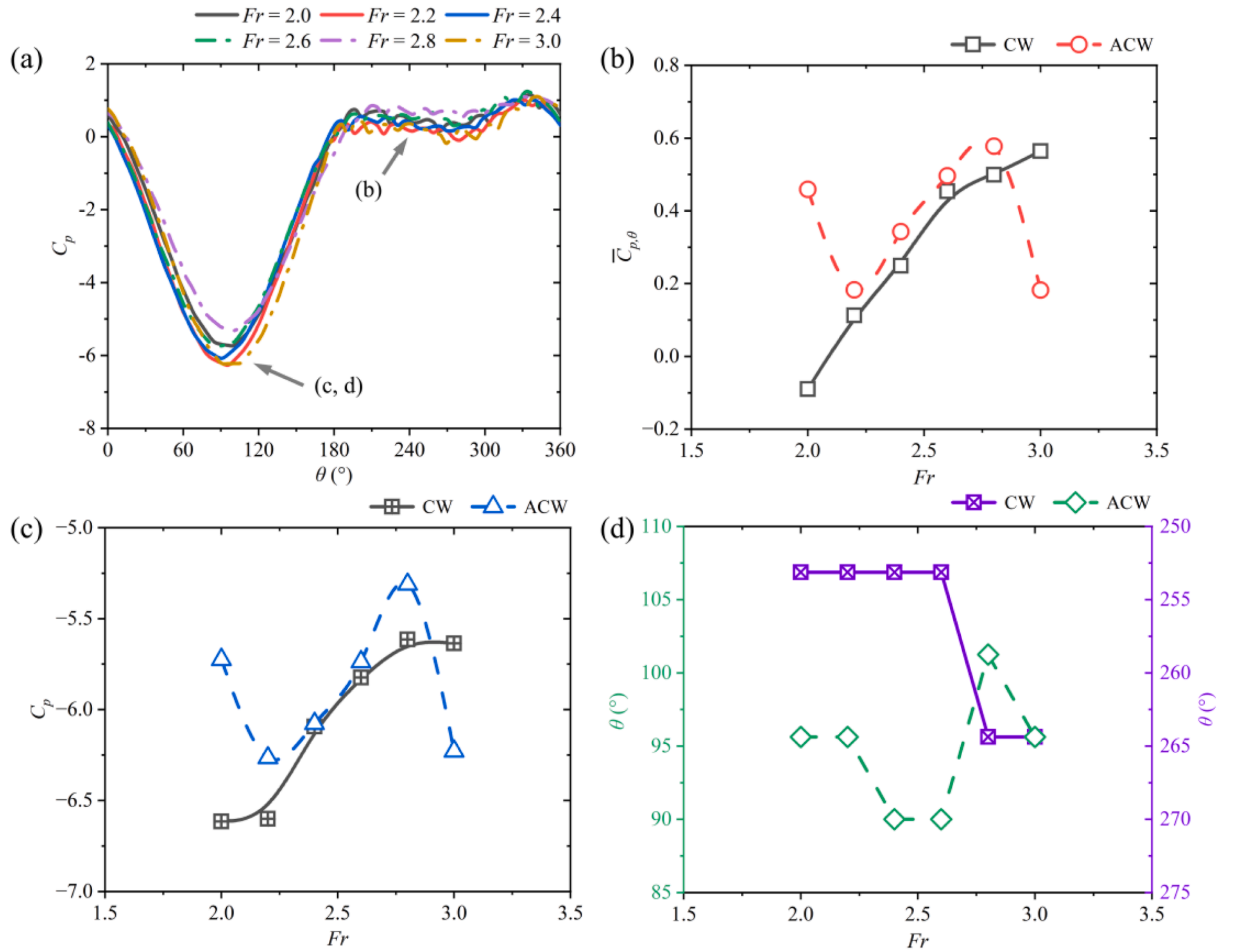

Fig. 15. Surface pressure coefficient distributions for the ACW rotating cylinder at different submergence depths for $H/D = 3$. (a) Instantaneous circumferential distribution of C_p, (b) angle-averaged pressure coefficient $\overline{C}_{p,\theta}$ evaluated over $\theta \in [180^{\circ}, 300^{\circ}]$, (c) minimum instantaneous C_p magnitude, and (d) circumferential angular position corresponding to the minimum instantaneous C_p.

and complex engineering applications.

CRediT authorship contribution statement

Jianfeng Lin: Writing – review & editing, Writing – original draft, Methodology, Investigation, Formal analysis. **Zenghui Zhu:** Validation, Data curation. **Xuxiang Cao:** Resources. **Lin Cai:** Investigation. **Shizhao Wang:** Supervision, Project administration, Conceptualization. **Hua-Dong Yao:** Writing – review & editing, Writing – original draft, Conceptualization.

Declaration of competing interest

The authors declare that they have no known competing financial interests or personal relationships that could have appeared to influence the work reported in this paper.

Acknowledgments

S.W. acknowledges support from the NSFC Excellence Research Group Program for 'Multiscale Problems in Nonlinear Mechanics' (grant number 12588201). J.L. acknowledges support from the National Natural Science Foundation of China (grant number 52501409) and the Postdoctoral Fellowship Program of CPSF (grant number GZB20240773). H.D.Y. acknowledges financial support by the Swedish Transport Administration in the SafeWinds project (Grant No TRV 2024/98491). The computations and data handling were enabled by resources provided by the National Academic Infrastructure for Supercomputing in Sweden (NAISS), partially funded by the Swedish Research Council through grant agreement no 2022-06725.

Appendix A. Mesh convergence study for the interface resolution

In this appendix, we present an analysis of the impact of interface resolution on the simulation results for a CW rotating cylinder in a two-phase flow. The study evaluates three different grid sizes under the conditions: $H/D = 3$ and $Fr = 3.2$. Table 4 summarises the key parameters and findings from the grid convergence study, including the C_l, C_d, and V_h/V_0 for the CW rotating cylinder. The mesh size near the free surface is always twice as large in the flow and spreading directions compared to the vertical direction. The relative errors of C_l, C_d, and V_h/V_0 show a trend of slight decreases with mesh refinement, and they converge to within 1% between the medium and fine mesh levels. Fig. 16 illustrates the morphological properties of the free surface for the three meshes. The wave profiles exhibit highly consistent shapes across the three resolutions, and the amplitude of the free-surface fluctuations demonstrates excellent convergence as the interface resolution increases, confirming the grid independence of the wave amplitude and interface morphology. Furthermore, to ensure the accurate quantification of air entrainment, the convergence of the dimensionless two-phase mixing volume and the total entrained gas volume was explicitly evaluated. The results indicate that the relative variations of these multiphase metrics between the medium and fine meshes are <0.5%. This confirms that the medium mesh provides a robust, grid-independent prediction of both the macroscopic free-surface deformation and the dispersed air entrainment dynamics. Given the extensive number of simulations required, a medium mesh was chosen as a practical compromise to limit computing time per simulation, taking into account factors such as processing power, memory capacity, and data storage capabilities.

Table 4
The results of the mesh convergence study for the interface resolution.

Mesh	1	2	3
Minimum Vertical cell size	$D/64$	$D/32$	$D/16$
Maximum vertical cell size	$D/32$	$D/16$	$D/8$
Total number of mesh cells (million)	90.13	35.28	28.67
C_l	4.684	4.687	4.680
Relative error of C_l (%)	–	0.06	0.09
C_d	0.526	0.523	0.520
Relative error of C_d (%)	–	0.52	1.25
V_h/V_0	109.693	110.505	111.190
Relative error of V_h/V_0 (%)	–	0.74	1.36

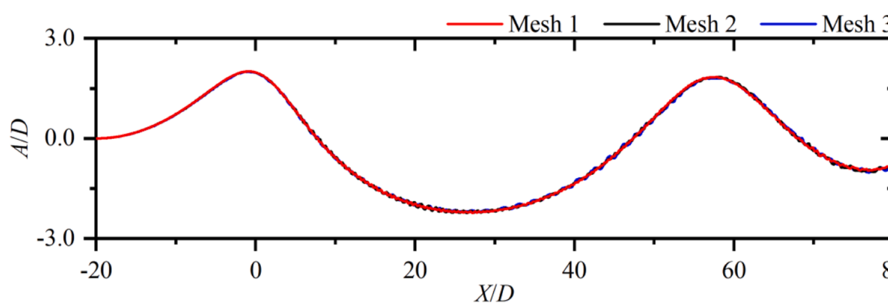

Fig. 16. Instantaneous morphological properties of the free surface influenced by the clockwise rotating cylinder at $H/D = 3$ and $Fr = 3.2$ with different interface resolutions.

Based on the medium mesh, additional statistical analyses are presented to demonstrate that the symmetry spanwise boundaries do not artificially constrain the turbulent structures. The spanwise correlation coefficient of the fluctuating spanwise velocity, $R(Y)$, is computed. The time-series data of the spanwise velocity were extracted from an array of probes distributed uniformly along the spanwise direction at $X/D = 0$ and $Z/D = 1.5$. As shown in Fig. 17, $R(Y)$ decays and approaches zero at $Y/D \approx 1$. Since the correlation length is significantly smaller than the half-domain width ($L/2D = 3.5$), it is confirmed that the large-scale three-dimensional turbulent structures are unconstrained by the symmetry boundaries.

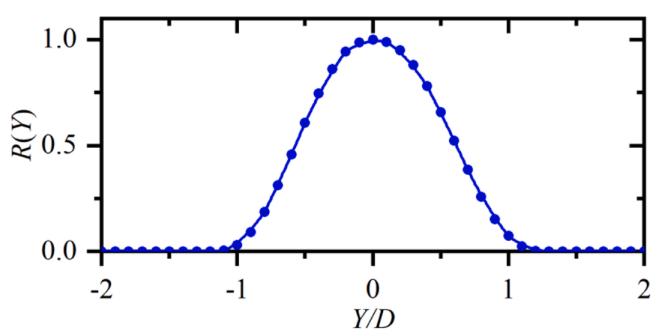

Fig. 17. Statistical diagnostics of the spanwise correlation coefficient of the fluctuating spanwise velocity, for evaluating spanwise boundary effects in the wake region.

Appendix B. Validation of the multiphase solver

To provide quantitative validation of the multiphase solver's capability to capture free-surface deformation, wave breaking, and air entrainment, additional benchmark comparisons are presented herein. For free-surface deformation, the present VOF method is validated against the recent DNS data of a stationary cylinder near a free surface reported by Sun et al. (2025). Fig. 18 presents a quantitative comparison of the dimensionless free-surface profile (vertical position Z/D versus streamwise position X/D). The numerical results demonstrate excellent agreement with the DNS data, accurately capturing both the upstream wave elevation and the downstream wave trough. The root-mean-square error in the wave amplitude between the numerical prediction and the DNS data is less than 3%, confirming the solver's high accuracy in resolving macroscopic interface deformation.

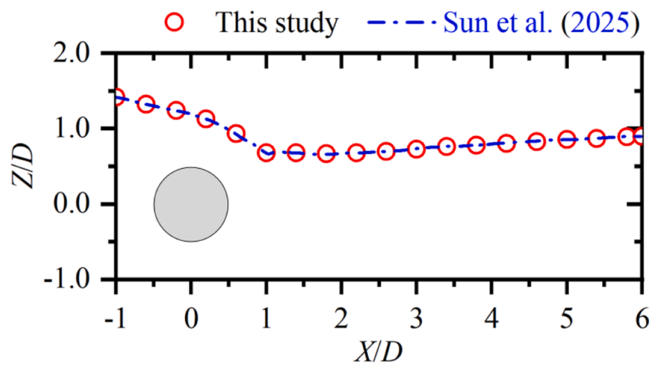

Fig. 18. Comparison of the dimensionless time-averaged free-surface profile versus streamwise position between the present VOF simulation and the DNS data of Sun et al. (2025) for a stationary cylinder near a free surface when $H/D = 1$, $Re = 2000$, $Fr = 1$, and $We = 1000$.

To validate the solver's robustness in capturing wave breaking and subsequent gas entrainment, the benchmark of three-dimensional breaking waves is simulated. Fig. 19 presents the dimensionless volume of entrained air V_α/V_c, calculated from the void fraction, as a function of normalised time t/T for a plunging breaker with wave slope of 0.55. The $V_c = A_c L_c$ is the reference maximum volume of air that can be entrained during the active breaking process, where A_c is the cross-sectional area of the entrained cylinder of air and L_c is the length of the breaking crest. The present VOF results show excellent agreement with the DNS data of Deike et al. (2016). The maximum entrained air volume differs by less than 5% between the present simulation and the reference DNS data.

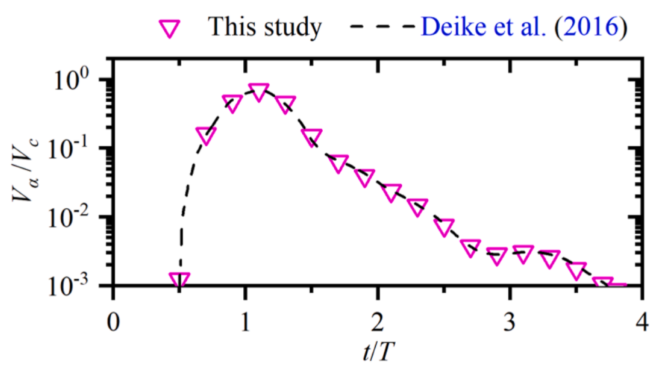

Fig. 19. Time evolution of the dimensionless entrained air volume V_α/V_c for a plunging breaker. Present VOF results compared with DNS data from Deike et al. (2016) at $Re = 4 \times 10^4$ and $Bo = 200$.

Data availability

Data will be made available on request.

References

Arya, N., De, A., 2019. Effect of grid sensitivity on the performance of wall adapting SGS models for LES of swirling and separating–reattaching flows. Comput. Math. Appl. 78 (6), 2035–2051. https://doi.org/10.1016/j.camwa.2019.03.038.

Aycan, O., Topuz, A., Kadem, L., 2023. Evaluating uncertainties in CFD simulations of patient-specific aorta models using grid convergence index method. Mech. Res. Commun. 133, 104188. https://doi.org/10.1016/j.mechrescom.2023.104188.

Baker, N., Kelly, G., O'Sullivan, P.D., 2020. A grid convergence index study of mesh style effect on the accuracy of the numerical results for an indoor airflow profile. Int. J. Vent. 19 (4), 300–314. https://doi.org/10.1080/14733315.2019.1667558.

Bourguet, R., 2021. Impact of body inclination on the flow past a rotating cylinder. J. Fluid Mech. 923, A33. https://doi.org/10.1017/jfm.2021.545.

Bouscasse, B., Colagrossi, A., Marrone, S., Souto-Iglesias, A., 2017. SPH modelling of viscous flow past a circular cylinder interacting with a free surface. Comput. Fluid. 146, 190–212. https://doi.org/10.1016/j.compfluid.2017.01.011.

Brackbill, J.U., Kothe, D.B., Zemach, C., 1992. A continuum method for modeling surface tension. J. Comput. Phys. 100 (2), 335–354. https://doi.org/10.1016/0021-9991(92)90240-Y.

Carstensen, S., Mandviwalla, X., Vita, L., Paulsen, U.S., 2014. Lift of a rotating circular cylinder in unsteady flows. J. Ocean Wind Energ. 1 (1), 41–49.

Chen, G.Q., Zhang, A.M., Huang, X., 2018. On the interaction between bubbles and the free surface with high density ratio 3D lattice Boltzmann method. Theor. Appl. Mech. Lett. 8 (4), 252–256. https://doi.org/10.1016/j.taml.2018.04.006.

Chen, W., Rheem, C.K., 2019. Experimental investigation of rotating cylinders in flow. J. Mar. Sci. Tech. 24, 111–122. https://doi.org/10.1007/s00773-018-0535-5.

Cheng, M., Luo, L.S., 2007. Characteristics of two-dimensional flow around a rotating circular cylinder near a plane wall. Phys. Fluid. 19 (6), 063601. https://doi.org/10.1063/1.2738608.

Cheng, W., Pullin, D.I., Samtaney, R., 2018. Large-eddy simulation of flow over a rotating cylinder: the lift crisis at $re_D=6\times10^4$. J. Fluid Mech. 855, 371–407. https://doi.org/10.1017/jfm.2018.644.

Choi, J., Yoon, S.B., 2009. Numerical simulations using momentum source wave-maker applied to RANS equation model. Coast. Eng. 56 (10), 1043–1060. https://doi.org/10.1016/j.coastaleng.2009.06.009.

Colagrossi, A., Nikolov, G., Durante, D., Marrone, S., Souto-Iglesias, A., 2019. Viscous flow past a cylinder close to a free surface: benchmarks with steady, periodic and metastable responses, solved by meshfree and mesh-based schemes. Comput. Fluid. 181, 345–363. https://doi.org/10.1016/j.compfluid.2019.01.007.

Daichin, Lee, S.J., 2004. POD analysis of near-wake structures of an elliptic cylinder adjacent to a free surface. J. Visual. 7 (3), 179–186. https://doi.org/10.1007/BF03181632.

Deike, L., Melville, W.K., Popinet, S., 2016. Air entrainment and bubble statistics in breaking waves. J. Fluid Mech. 801, 91–129. https://doi.org/10.1017/jfm.2016.372.

Ferro, P., Landel, P., Landrodie, C., Guillot, S., Pescheux, M., 2025. Enhanced level-set method for free surface flow applications. Int. J. Multiphas. Flow 185, 105126. https://doi.org/10.1016/j.ijmultiphaseflow.2025.105126 doi.org/105126.

Feshalami, B.F., He, S., Scarano, F., Gan, L., Morton, C., 2022. A review of experiments on stationary bluff body wakes. Phys. Fluids 34 (1), 011301. https://doi.org/10.1063/5.0077323.

Gu, M., Song, B., Zhang, B., Mao, Z., Tian, W., 2020. The effects of submergence depth on vortex-induced vibration (VIV) and energy harvesting of a circular cylinder. Renew. Energ. 151, 931–945. https://doi.org/10.1016/j.renene.2019.11.086.

Hirt, C.W., Nichols, B.D., 1981. Volume of fluid (VOF) method for the dynamics of free boundaries. J. Comput. Phys. 39 (1), 201–225. https://doi.org/10.1016/0021-9991(81)90145-5.

Hu, T., Ren, H., Shen, J., Niu, Z., Zhang, M., Xu, Y., Song, B., Sun, T., 2023. Experimental investigation on hydrodynamic forces of semi-submerged cylinders in combined

steady flow and oscillatory flow. Ocean Eng. 268, 113612. https://doi.org/10.1016/j.oceaneng.2022.113612.
Kim, M., Lim, J., Kim, S., Jee, S., Park, D., 2020. Assessment of the wall-adapting local eddy-viscosity model in transitional boundary layer. Comput. Method. Appl. M. 371, 113287. https://doi.org/10.1016/j.cma.2020.113287.
Kumar, P., Das, A.K., Mitra, S.K., 2017. Air entrainment driven by a converging rotational field in a viscous liquid. Phys. Fluids 29 (10), 102104. https://doi.org/10.1063/1.4991763.
Lin, J., Guo, C., Zhao, D., Han, Y., Su, Y., 2022. Hydrodynamic simulation for evaluating Magnus anti-rolling devices with varying angles of attack. Ocean Eng. 260, 111949. https://doi.org/10.1016/j.oceaneng.2022.111949.
Lin, J., Han, Y., Su, Y., Zhang, Z., 2021. Magnus antirolling system for ships at zero speed. IEEE T. Transp. Electr. 7 (4), 3062–3069. https://doi.org/10.1109/TTE.2021.3082946.
Lin, J., Wang, S., Yao, H.-D., Su, Y., 2024. Intelligent control of the Magnus anti-rolling device: a co-simulation approach. Ocean Eng. 312, 119304. https://doi.org/10.1016/j.oceaneng.2024.119304.
Lin, J., Yao, H.-D., 2023. Modified magnus effect and vortex modes of rotating cylinder due to interaction with free surface in two-phase flow. Phys. Fluid. 35 (5), 123614. https://doi.org/10.1063/5.0179744.
Lin, J., Yao, H.-D., Han, Y., Su, Y., Zhang, C., 2023. Shape optimization and hydrodynamic simulation of a Magnus anti-rolling device based on fully parametric modeling. Phys. Fluid. 35 (5), 055136. https://doi.org/10.1063/5.0152179.
Lu, L., Qin, J.M., Teng, B., Li, Y.C., 2011. Numerical investigations of lift suppression by feedback rotary oscillation of circular cylinder at low reynolds number. Phys. Fluids 23, 033601. https://doi.org/10.1063/1.3560379.
Malavasi, S., Guadagnini, A., 2007. Interactions between a rectangular cylinder and a free-surface flow. J. Fluid. Struct. 23 (8), 1137–1148. https://doi.org/10.1016/j.jfluidstructs.2007.04.002.
Mittal, S., Kumar, B., 2003. Flow past a rotating cylinder. J. Fluid Mech. 476, 303–334. https://doi.org/10.1017/S0022112002002938.
Munir, A., Zhao, M., Wu, H., Lu, L., 2019. Numerical investigation of wake flow regimes behind a high-speed rotating circular cylinder in steady flow. J. Fluid Mech. 878, 875–906. https://doi.org/10.1017/jfm.2019.677.
Panda, S.K., Rana, B.K., 2022. Numerical simulation and analytical prediction on the development of entrained air filament caused by the combined effect of rotational field and free stream flow. Ind. Eng. Chem. Res. 61 (26), 9456–9473. https://doi.org/10.1021/acs.iecr.2c00684.
Panda, S.K., Rana, B.K., Kumar, P., 2022. Entrainment in multifluid systems, and rotation induced occurrences. Eur. J. Mech. B-Fluid. 96, 156–172. https://doi.org/10.1016/j.euromechflu.2022.08.001.
Park, S., Oh, G., Rhee, S.H., Koo, B.Y., Lee, H., 2015. Full scale wake prediction of an energy saving device by using computational fluid dynamics. Ocean Eng. 101, 254–263. https://doi.org/10.1016/j.oceaneng.2015.04.005.
Patel, K., Sun, J., Yang, Z., Zhu, X., 2025. Coupled liquid–gas flow over a submerged cylinder: interface topology, wake structure and hydrodynamic lift. J. Fluid Mech. 1008, A10. https://doi.org/10.1017/jfm.2025.162.
Pralits, J.O., Brandt, L., Giannetti, F., 2010. Instability and sensitivity of the flow around a rotating circular cylinder. J. Fluid Mech. 650, 513–536. https://doi.org/10.1017/S0022112009993764.
Radi, A., Thompson, M.C., Rao, A., Hourigan, K., Sheridan, J., 2013. Experimental evidence of new three-dimensional modes in the wake of a rotating cylinder. J. Fluid Mech. 734, 567–594. https://doi.org/10.1017/jfm.2013.486.
Rana, B.K., Das, A.K., Das, P.K., 2016. Numerical study of air entrainment and liquid film wrapping around a rotating cylinder. Ind. Eng. Chem. Res. 55 (46), 11950–11960. https://doi.org/10.1021/acs.iecr.6b03477.
Rao, A., Leontini, J.S., Thompson, M.C., Hourigan, K., 2013. Three-dimensionality in the wake of a rapidly rotating cylinder in uniform flow. J. Fluid. Mech. 730, 379–391. https://doi.org/10.1017/jfm.2013.362.
Rao, A., Radi, A., Leontini, J.S., Thompson, M.C., Sheridan, J., Hourigan, K., 2015. The influence of a small upstream wire on transition in a rotating cylinder wake. J. Fluid. Mech. 769, R2. https://doi.org/10.1017/jfm.2015.152.
Reichl, P., Hourigan, K., Thompson, M.C., 2005. Flow past a cylinder close to a free surface. J. Fluid. Mech. 533, 269–296. https://doi.org/10.1017/S0022112005004209.
Ren, H., Xu, Y., Zhang, M., Deng, S., Li, S., Fu, S., Sun, H., 2019. Hydrodynamic forces on a partially submerged cylinder at high Reynolds number in a steady flow. Appl. Ocean Res. 88, 160–169. https://doi.org/10.1016/j.apor.2019.04.025.
Rodriguez, I., Lehmkuhl, O., Piomelli, U., Chiva, J., Borrell, R., Oliva, A., 2017. LES-based study of the roughness effects on the wake of a circular cylinder from subcritical to transcritical reynolds numbers. Flow Turbul. Combust. 99 (3), 729–763. https://doi.org/10.1007/s10494-017-9866-2.
Seifert, J., 2012. A review of the Magnus effect in aeronautics. Prog. Aerosp. Sci. 55, 17–45. https://doi.org/10.1016/j.paerosci.2012.07.001.
Sharma, Y., Rana, B.K., Das, A.K., 2015. Rotary entrainment in two phase stratified gas-liquid layers: an experimental study. Int. J. Chem. Mol. Eng. 9 (12), 1367–1372.
Sun, J., Lu, M., Patel, K., Zhu, X., Yang, Z., 2025. Free-surface flow past a submerged horizontal cylinder: reynolds-number dependence. J. Fluid. Mech. 1023, A39. https://doi.org/10.1017/jfm.2025.10839.
Swanson, W.M., 1961. The Magnus effect: a summary of investigations to date. J. Basic Eng. 83, 461–470. https://doi.org/10.1115/1.3659004.
Wacławczyk, T., Koronowicz, T., 2008. Comparison of CICSAM and HRIC high-resolution schemes for interface capturing. J. Theor. App. Mech. 46 (2), 325–345.
Zhao, F., Wang, R., Zhu, H., Cao, Y., Bao, Y., Zhou, D., Cheng, B., Han, Z., 2024. Free-surface effects on the flow around two circular cylinders in tandem. J. Fluid Mech. 1001, A7. https://doi.org/10.1017/jfm.2024.1066.
Zhao, F., Wang, R., Zhu, H., Ping, H., Bao, Y., Zhou, D., Cao, Y., Cui, H., 2021. Large-eddy simulations of flow past a circular cylinder near a free surface. Phys. Fluid. 33 (11), 115108. https://doi.org/10.1063/5.0068193.
Zhou, H., Xiang, M., Zhao, S., Zhang, W., 2019. Development of a multiphase cavitation solver and its application for ventilated cavitating flows with natural cavitation. Int. J. Multiphas. Flow 115, 62–74. https://doi.org/10.1016/j.ijmultiphaseflow.2019.03.020.